Supplementary Materials

Synthesis and microstructural properties of Pt-decorated α-Fe_2O_3 nanotubes for hydrogen gas sensing applications

Monika Šoltić[1], Maria Gracheva[2,3], Nikola Baran[1], Goran Dražić[4], Robert Peter[5], Károly Lázár[2], Goran Štefanić[1], Marijan Marciuš[6], Nikolina Novosel[7], László Ferenc Kiss[8], Matthijs A. van Spronsen[9], Mile Ivanda[1], Zoltán Klencsár[2,*], Marijan Gotić[1,*]

[1]Laboratory for Molecular Physics and Synthesis of New Materials, Division of Materials Physics, Ruđer Bošković Institute, Bijenička cesta 54, 10 000 Zagreb, Croatia
[2]Budapest Neutron Centre, Institute for Energy Security and Environmental Safety, HUN-REN Centre for Energy Research, Konkoly-Thege Miklós út 29-33, Budapest 1121, Hungary
[3]Institute of Chemistry, ELTE Eötvös Loránd University, Pázmány Péter s. 1/A, 1117 Budapest, Hungary
[4]National Institute of Chemistry, Hajdrihova, 19, SI-1001, Ljubljana, Slovenia
[5]University of Rijeka, Faculty of Physics and Centre for Micro- and Nanosciences and Technologies, Radmile Matejčić 2, Rijeka, Croatia
[6]Laboratory for the synthesis of new materials, Division of Materials Chemistry, Ruđer Bošković Institute, 10000 Zagreb, Croatia
[7]Institute of Phisics, Bijenička cesta 46, 10000 Zagreb, Croatia
[8]Institute for Solid State Physics and Optics, HUN-REN Wigner Research Centre for Physics, Konkoly-Thege Miklós út 29-33, Budapest 1121, Hungary
**Corresponding authors: gotic@irb.hr (M. Gotić), klencsar.zoltan@ek.hun-ren.hu (Z. Klencsár)*

Table of contents:

Figure. S8 Fe $L_{2,3}$ edge NEXAFS spectra of T-FP0, T-FP0$_{ann}$, T-FP1 and T-FP5.

Figure. S9 Quantitative distribution of oxygen species (%) in the synthesized samples.

Figure. S10 TGA thermogram of the T-FP0 sample.

Figure. S11 Combined TGA-DSC diagram of T-FP0, showing the TGA curve, the DTG curve and the DSC curve.

Figure. S12 Room temperature ^{57}Fe Mössbauer spectra of samples T-FP0, T-FP1 and T-FP5.

Figure. S13 Hyperfine magnetic field distributions in samples T-FP0, T-FP1 and T-FP5, as derived from the room temperature ^{57}Fe Mössbauer spectra shown in Figure S12.

Table. S4 Room temperature ^{57}Fe Mössbauer parameters of hematite nanotube samples T-FP0, T-FP1 and T-FP5 obtained via simultaneous fitting of the spectra shown in Figure S12.

Figure. S14 ^{57}Fe Mössbauer spectrum (black dots) of sample T-FP1 recorded at 150 K, along with its decomposition and fit envelope (solid lines).

Table. S5 ^{57}Fe Mössbauer parameters of the hematite nanotube sample T-FP1 at 150 K.

Figure. S15 Low-temperature (T = 87-88 K) ^{57}Fe Mössbauer spectra of samples T-FP0, T-FP1 and T-FP5.

Table. S6 Low temperature (T = 87-88 K) ^{57}Fe Mössbauer parameters of hematite nanotubes with and without platinum decoration.

Figure. S16 Comparison of the EPR spectra of T-FP0, T-FP1 and T-FP5 measured at 150 K and 290 K.

Figure. S17 Temperature dependence of the X-band EPR spectra of samples T-FP0, T-FP1 and T-FP5 recorded between 150 K and 290 K.

Figure. S18 First integral of the respective EPR signals displayed in Figure S13, showing the magnetic field dependence of the A microwave absorption.

Table. S7 Average baseline electrical resistance (R_0) of T-FP0, T-FP0$_{ann}$, T-FP1 and T-FP5 samples measured in air and nitrogen at 363, 463 and 553 K.

Figure. S19 Schematic illustration of the proposed gas sensing mechanism for an n-type semiconducting metal oxide in air and upon exposure to hydrogen.

Table. S8 Comparative overview of hydrogen sensing performance reported for various metal-oxide semiconductor (MOS)–based hydrogen sensors.

Figure. S20 Average response time (fall time) of the electrical resistance for T-FP0, T-FP0$_{ann}$, T-FP1 and T-FP5 samples measured in air at different temperatures.

Figure. S21 Comparison of 1 mol% Pt-decorated α-Fe_2O_3 samples with nanotubes and irregular morphology from Šoltić et al.[1]

Figure. S22 Comparison of 5 mol% Pt-decorated α-Fe_2O_3 samples with nanotube and irregular morphologies from Šoltić et al.[1]

Figure. S23 Gas (N_2) adsorption and desorption isotherms and calculated BET surface areas of the synthesized samples.

Figure. S24 Comparison of the response of sample T-FP0 to hydrogen gas, measured in air and nitrogen atmospheres.

Figure. S25 Comparison of the response of sample T-$FP0_{ann}$ to hydrogen gas, measured in air and nitrogen atmospheres.

S1. Experimental

S1.1. Characterization techniques

S1.1.1. Structural and elemental analysis

A thermal field emission scanning electron microscope (FE-SEM), model JSM-7000F (JEOL Ltd.), coupled with an energy dispersive X-ray analyzer EDS/INCA 350 (Oxford Instruments), was used to analyze the morphology of the samples. For more detailed morphological and elemental composition analyses, an atomic resolution scanning transmission electron microscope (AR STEM), model JEOL ARM 200 CF, operating at 80 kV and coupled with a Gatan Quantum ER EELS system, and energy dispersive X-ray spectrometry (EDS) (JEOL Centurio 100, Tokyo, Japan), was used.

S1.1.2. XRD measurements

X-ray diffraction (XRD) measurements were performed at room temperature using a Malvern PANalytical Empyrean diffractometer equipped with a CuKα radiation source, appropriate monochromator and detector systems, manufactured by Malvern PANalytical B.V., Almelo, The Netherlands.

S1.1.3. XPS measurements

X-ray photoelectron spectroscopy (XPS) was used to investigate the oxidation states of Fe and Pt and the chemical bonding of O in the samples T-FP0, T-$FP0_{ann,}$ T-FP1 and T-FP5. Spectra around the Fe 2p, Pt 4f and O 1s core levels were obtained using a SPECS instrument under ultra-high vacuum (UHV) conditions, with the pressure in the analytical chamber maintained at approximately 10^{-7} Pa. Al Kα X-rays with an energy of 1486.74 eV served as the excitation source, and the Phoibos100 electron energy analyzer was used for data acquisition. To stabilize surface charge on the non-conductive oxide samples during XPS analysis, 5 eV electrons were flooded onto the sample surface. The pass energy was set to 50 eV for the Pt 4f spectra, while the Fe 2p and O 1s spectra were measured with a pass energy of 20 eV. After subtracting a Shirley

background, numerical fitting of the experimental data was performed with Unifit software[2] using a product of Gaussian and Lorentz functions. All photoemission spectra were calibrated to the C 1s peak, which was set to a binding energy (BE) of 284.5 eV.

S1.1.4. NEXAFS measurements

Near-edge X-ray absorption fine structure (NEXAFS) measurements of the Fe $L_{2,3}$ and O K edges, the samples were pressed into carbon tape. These were then loaded into the "TPOT" endstation of beamline B07c at the Diamond Light Source.[3] X-rays from the bending-magnet source were monochromatized with a 600-l/mm plane grating, exit slits set to 0.025 mm, and a C_{ff} of 2. Spectra were collected using electron yield by measuring the drain current of the hemispherical analyzer cone. To mitigate charging, the chamber was filled with 5 mbar He (Air Products BIP®, 6.0 N purity) delivered using a mass flow controller in a dedicated gas handling system.[4] Spectra were collected at room temperature. For each sample, four spots (two for Fe $L_{2,3}$ and two for O K) were measured and each scan was repeated twice. Spectra were normalized by the ring current and shifted in energy, so that the Fe_2O_3 white line is at 708.9 eV, matching previously reported spectra.[5]

S1.1.5. TGA/DSC analysis

Thermogravimetric analysis was conducted in the temperature range of 35 to 1000°C at a heating rate of 10°C min^{-1} in a nitrogen atmosphere. Aluminum oxide crucibles with a volume of 150 µL were used and the sample mass ranged from 10 to 15 mg. The analysis was performed using a Mettler Toledo TGA/DSC 3+ instrument. The instrument was also equipped with DSC sensors whose signals provided additional insight into the reaction.

S1.1.6. Mössbauer spectroscopy

^{57}Fe Mössbauer spectra were recorded in transmission geometry using a standard WissEl Mössbauer spectrometer setup (Starnberg, Germany) with a ^{57}Co(Rh) radioactive source at an activity of ~5 mCi. Circular absorbers with a diameter of 15.5 mm were prepared by mixing 25 mg of each sample with 100 mg of cellulose. For room temperature ($T \approx 290$ K) measurements, the source movement followed a sinusoidal velocity signal. Unfolded spectra were recorded in 2048 channels and subsequently folded into 1024 channels for further processing.

For low temperature ($T = 87$-88 K) measurements, separate circular absorbers with a diameter of 16 mm were prepared using either 5-6 mg or 25 mg of each sample, mixed with cellulose powder. The samples were placed in a bath type cryostat with temperature control (SVT-400-MOSS, Janis, Woburn, MA, USA) filled with liquid nitrogen, while the spectrometer operated in constant acceleration mode with a triangular velocity waveform, recording spectra in 512 channels before folding.

The Mössbauer spectra were evaluated by applying Voigt based fitting[6] as implemented in the MossWinn program, assuming that the ^{57}Fe hyperfine magnetic field is subject to a Gaussian

distribution for each fitted subcomponent. The isomer shifts are given relative to that of α-Fe at room temperature.

S1.1.7. Electron paramagnetic resonance

X-band electron paramagnetic resonance (EPR) measurements were performed using a Bruker ElexSys E500 X-band spectrometer. Approximately 5 mg of sample was thoroughly mixed with 200 mg of KBr powder and loaded into Wilmad-LabGlass 710-SQ-250M quartz sample tubes. The Wilmad-LabGlass WG-821-F-Q variable temperature insert was used, with temperature controlled by flow-through of cryogenically cooled nitrogen gas, to conduct measurements in the temperature range of T = 150-290 K. The EPR measurement conditions included a modulation frequency of 100 kHz, a modulation amplitude of 5 G and a microwave power of ~ 20.7 mW. EPR spectra, proportional to the first derivative of the microwave absorption with respect to the sweeping magnetic field, were recorded in 2048 channels over a magnetic field range of 100-10900 G with a sweep time of ~ 84 s. The results of two scans were averaged for each measurement. The microwave frequency was $f \approx 9.31$ GHz. The B (applied magnetic field) axis of the spectra was rescaled to the common frequency of $f_0 = 9.31$ GHz (i.e., B abscissa values were multiplied by f_0/f). Baseline correction was applied to all spectra before analysis and further processing.

S1.1.8. Magnetic measurements

The powder samples were placed in a gelatin capsule. Magnetic measurements were performed using a Quantum Design MPMS-5 SQUID magnetometer in the temperature range of 5–300 K and magnetic field range of 0–5 T. The temperature dependence of magnetization at a small field (H = 100 Oe) was measured during warming to room temperature (RT) after cooling the sample in zero field (ZFC), followed by measurement during cooling at the same field down to T = 5 K (FCC), and then during warming at the same field up to RT (FCW).

AC magnetic susceptibility was measured using a Cryobind high-precision AC susceptibility measurement system. Measurements were performed in the temperature range 4.2–315 K using an AC driving field with amplitude 3.2 Oe and frequency 231 Hz, with compensation for Earth's magnetic field.

S1.2. Gas sensing measurements

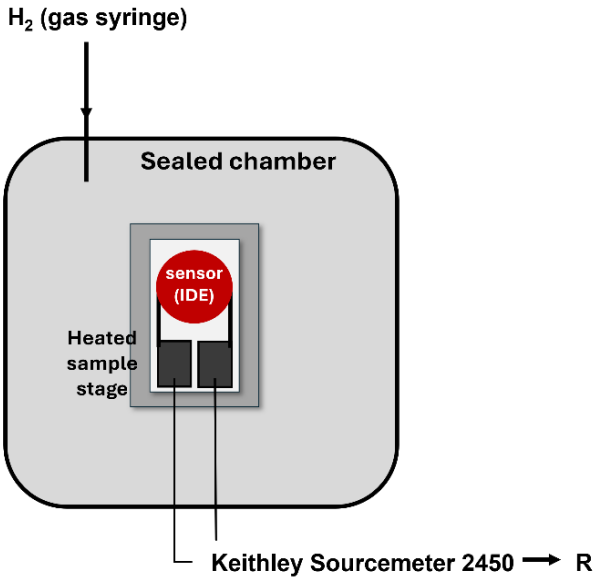

Figure S1. Schematic illustration of the custom-built sealed gas sensing chamber used for hydrogen measurements. The sensor (IDE) is placed on a heated sample stage with controlled temperature, while hydrogen is introduced into the sealed chamber using a calibrated gas syringe. Electrical connections to a Keithley source meter enable resistance measurements under controlled conditions.

S2. Results and discussion

S2.1. Structural and elemental results

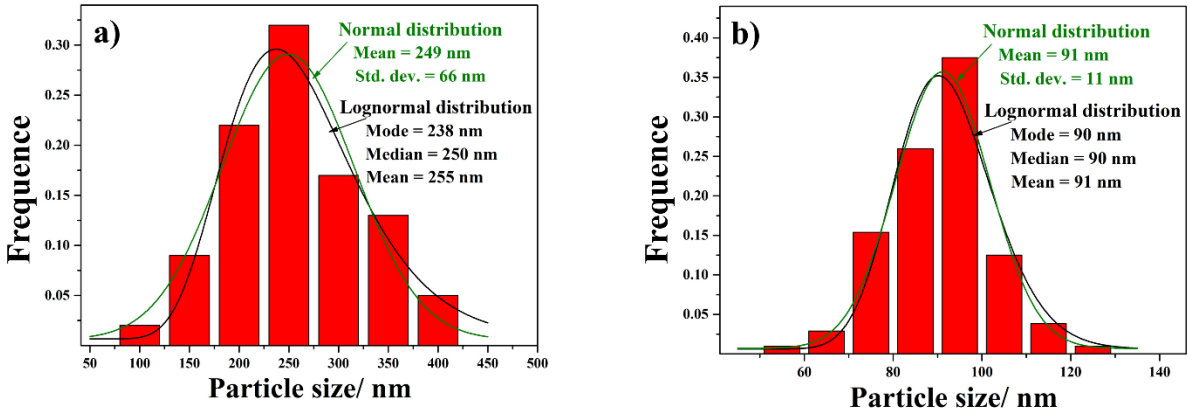

Figure S2. Statistical distributions of α-Fe_2O_3 nanotube length (a) and width (b), obtained from FE-SEM image analysis.

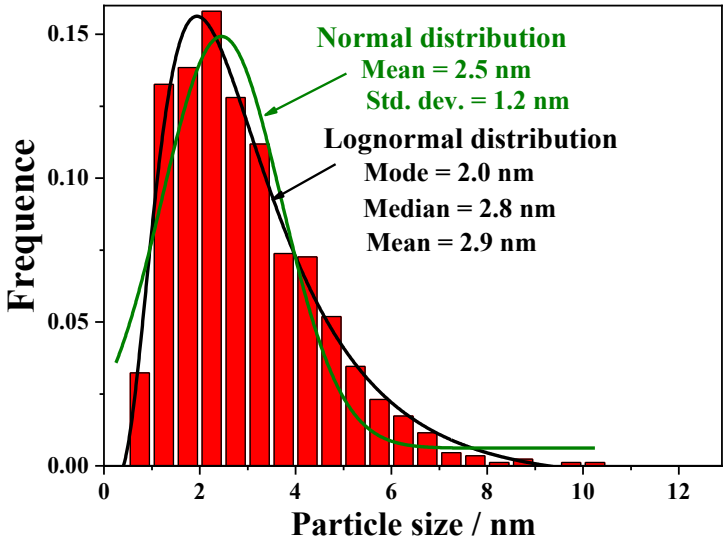

Figure S3. Statistical size distribution of platinum nanoparticles in the T-FP5 sample, obtained from STEM image analysis.

The elemental composition of the samples was determined using field emission scanning electron microscopy coupled with energy dispersive spectroscopy (FESEM/EDS). The results, presented in Table S1, show accurate and reproducible measurements of the elemental composition.

The EDS results indicate that the platinum content in the T-FP1 and T-FP5 samples matches the target values of 1 mol% and 5 mol%, as shown by the measured atomic percentages of Pt (0.25 at% for T-FP1 and 1.10 at% for T-FP5). The higher oxygen content in the T-FP5 sample (88.00 at%) compared to T-FP1 (82.00 at%) may be due to surface oxidation or structural changes resulting from the increased platinum concentration.

Phosphorus (P) was also detected in both samples, with an average atomic percentage of about 0.85 at% in T-FP1 and 0.90 at% in T-FP5. The presence of phosphorus is attributed to the use of ammonium dihydrogen phosphate ($NH_4H_2PO_4$) as a precursor in the synthesis. Although phosphorus is not a major component, its presence may influence the surface chemistry and possibly contribute to the magnetic properties.

Table S1. Elemental composition (wt% and at%) of samples T-FP1 and T-FP5, determined by FESEM/EDS analysis. The table shows average values calculated from measurements at several points for each sample.

Sample	Iron (Fe) wt%	Oxygen (O) wt%	Platinum (Pt) wt%	Phosphorus (P) wt%	Iron (Fe) at%	Oxygen (O) at%	Platinum (Pt) at%	Phosphorus (P) at%
T-FP1	48.91	49.52	1.34	1.25	16.10	82.00	0.25	0.85
T-FP5	37.34	61.88	6.49	1.16	10.00	88.00	1.10	0.90

S2.2. XRD results

S2.2.1. Quantitative analysis and line broadening

Figure S4. shows powder X-ray diffractograms of T-FP0$_{ann}$, T-FP1 and T-FP5. The corresponding *hkl* (Miller) indices of the α-Fe_2O_3 phase, indexed according to ICDD PDF card No. 33-0664, as well as the positions of Pt diffraction peaks, are shown in Figure S5. The diffraction patterns of all samples show peaks corresponding to α-Fe_2O_3, confirming hematite as the single phase. The first signs of platinum diffraction lines appear in sample T-FP1, indicating that platinum has no solubility in the hematite lattice.

The weighted-profile R-factor (R_{wp}) values indicate good agreement between the observed and calculated patterns for all samples, confirming the phase composition and crystallinity. The diffraction lines of hematite are narrow in all samples, further confirming its excellent crystallinity. However, this narrowness makes it difficult to accurately determine the size of the crystalline domains based on line broadening. The volume-averaged domain size (Dv) of the hematite phase was estimated to be about 100 nm, while the domain size of the platinum phase in the T-FP5 sample was estimated to be about 6.6(1) nm based on Rietveld refinement. Although the average Pt nanoparticle size determined by TEM is ~2.5 ± 1.2 nm, the larger value determined by XRD (6.6 nm) reflects only the contribution of the larger crystalline domains. This discrepancy is arises because X-ray diffraction is less sensitive to very small and highly dispersed nanoparticles, which make only a weak or no contribution to the diffraction pattern. Therefore, the XRD result represents a volume-averaged size of the larger Pt particles, whereas TEM provides a more accurate assessment of the overall particle size distribution.

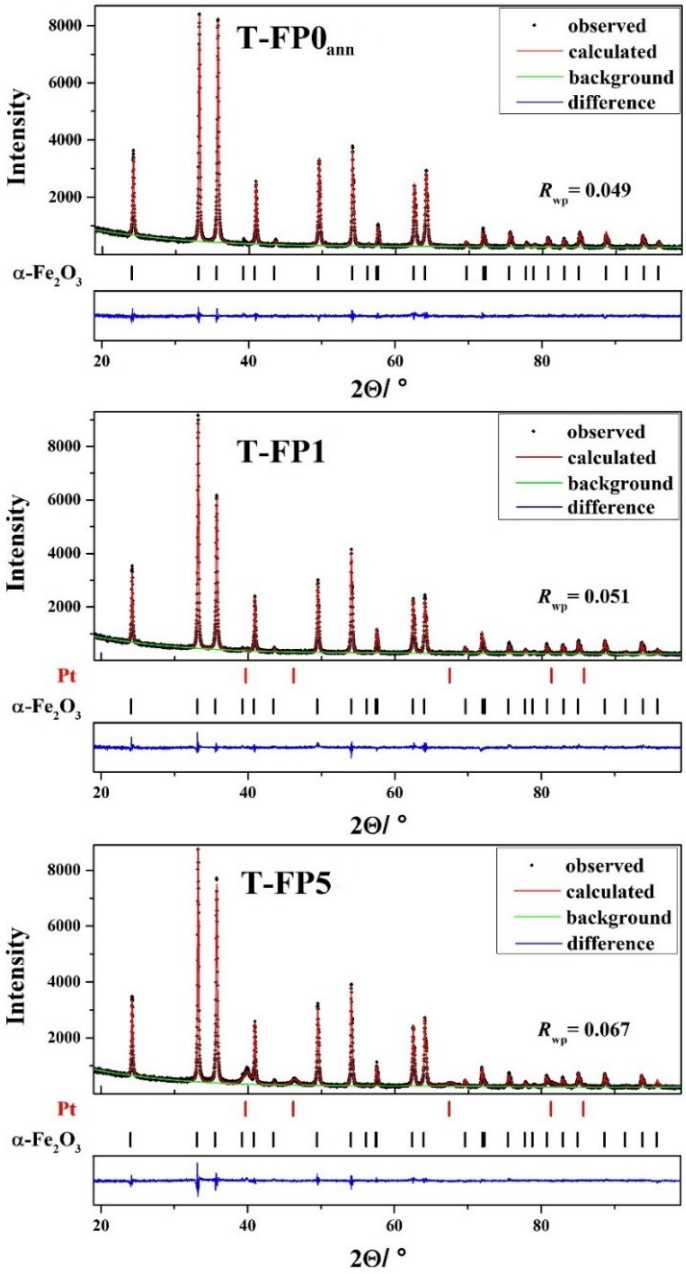

Figure S4. X-ray diffraction (XRD) patterns for the samples T-FP0$_{ann}$, T-FP1, and T-FP5. The observed diffraction data (black dots) are fitted to the calculated patterns (red lines), with the difference curve shown in blue. The positions of the characteristic peaks for α-Fe_2O_3 and Pt are marked with black and red ticks, respectively.

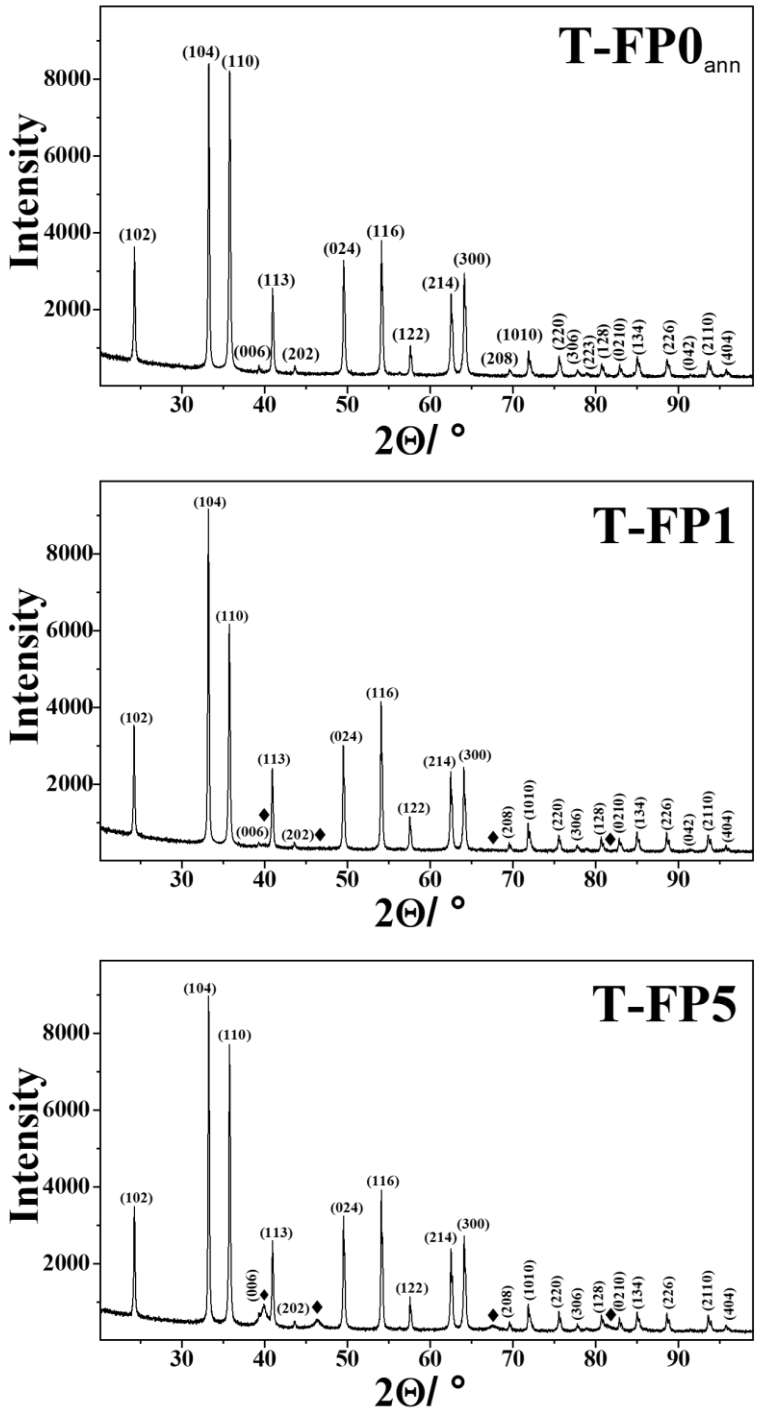

Figure S5. X-ray diffraction (XRD) patterns for the samples T-FP0$_{ann}$, T-FP1, and T-FP5. The diffraction peaks of the α-Fe_2O_3 phase are indexed with the corresponding *hkl* (Miller) indices according to ICDD PDF card No. 33-0664. The symbol ♦ indicates the positions of Pt diffraction peaks with *hkl* indices (111) at 39.8° 2θ, (200) at 46.3° 2θ, (220) at 67.5° 2θ, and (311) at 81.4° 2θ.

S2.2.2. Lattice parameters determination

Table S2. shows the results of the Rietveld refinement of the powder diffraction patterns, which indicate that the presence of platinum has only a minor or negligible effect on the unit cell parameters of the hematite phase in the samples. A slightly larger c-parameter was observed for the Pt-free hematite sample (T-FP0), which was attributed to the absence of thermal treatment rather than the presence of platinum. After sample T-FP0 was subjected to the same thermal treatment as the platinum-containing samples (resulting in sample T-FP0$_{ann}$), there was a slight shortening of the c parameter, making its value very similar to that of the platinum-containing samples.

Table S2. Refined values of the lattice parameters and unit cell volume of the hematite phase in samples T-FP0, T-FP0$_{ann}$, T-FP1 and T-FP5, determined from the Rietveld refinement results (MAUD program) of XRD patterns.

Sample	x(Pt)	Lattice parameters		V / nm^3
		a / nm	c / nm	
T-FP0	0	0.50347(1)	1.37896(3)	0.3495(1)
T-FP0$_{ann}$	0	0.50343(1)	1.37828(3)	0.3494(1)
T-FP1	0.01	0.50348(1)	1.37825(4)	0.3494(1)
T-FP5	0.05	0.50349(1)	1.37840(2)	0.3494(1)

S2.3. XPS results

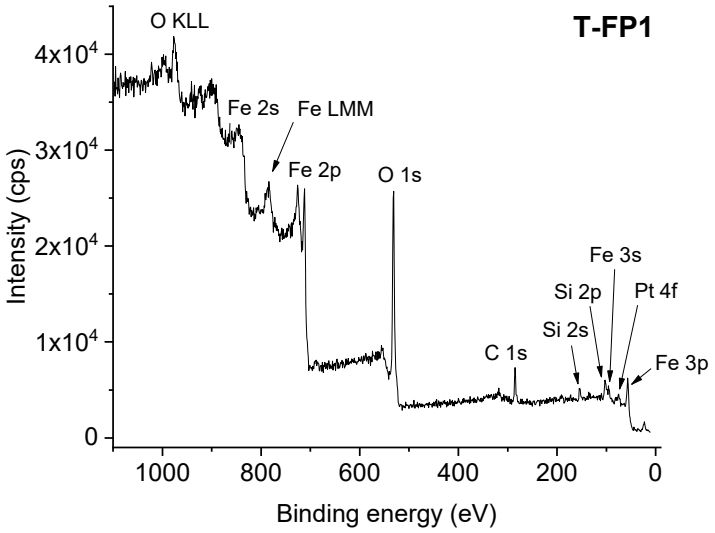

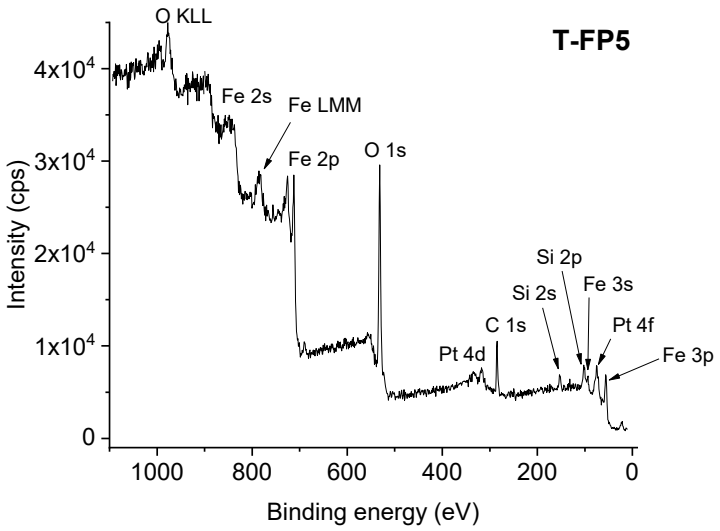

Figure S6. Wide-scan XPS spectra of samples T-FP1 (left) and T-FP5 (right) with labeled core-level peaks. The spectra confirm the presence of Fe, O and Pt in the samples, along with minor contributions from C and Si. These results provide an overview of the elemental composition of the samples and confirm the successful incorporation of platinum on the surfaces of the hematite nanotubes.

The presence of carbon in the XPS elemental analysis (Figure S6, Table 2) is primarily due to the use of organic compounds during the synthesis process. Specifically, platinum (II) acetylacetonate ($Pt(acac)_2$) was used as the Pt precursor and dissolved in 5 mL of toluene. Both acetylacetonate and toluene are potential sources of residual carbon, especially at the sample surface area analyzed by XPS. Therefore, the relatively high atomic percentage of carbon detected by XPS reflects surface-bound carbonaceous residues originating mainly from toluene. This is an inherent limitation of the synthesis approach; however, it should be emphasized that the hydrothermal method combined with Pt decoration offers several key advantages, including controlled morphology and uniform Pt distribution, which contribute significantly to improved gas sensing performance.

S.2.3.1. Pt 4f-XPS spectra

The $4f_{7/2}$ peaks appear at binding energies of 70.8 ± 0.1 eV (Pt^0), 72.5 ± 0.1 eV (Pt^{2+}) and 74.5 ± 0.1 eV (Pt^{4+}), while the full width at half maximum (FWHM) of all Pt 4f peaks is (2.5 ± 0.1) eV (Fig. 4). The intensity ratio between the $4f_{5/2}$ and $4f_{7/2}$ peaks is (0.75 ± 0.05), and the energy separation between these peaks is (3.40 ± 0.05) eV, in good agreement with literature values and consistent with our previous work on $Pt/MnO_4/Mn_5O_8$.[7] The presence of all three oxidation states can be attributed to surface and interfacial effects. Metallic Pt^0 forms through thermal decomposition of the $Pt(acac)_2$ precursor during annealing, while Pt^{4+} may result from surface oxidation of Pt^0 due to adsorption of molecular oxygen and interactions with hydroxyl groups and water molecules on the hematite surface.

Table S3. Average oxidation state of platinum (Pt) in samples T-FP1 and T-FP5, calculated from the deconvoluted Pt 4f XPS spectra*.

Sample	Average oxidation state of Pt
T-FP1	2.01
T-FP5	2.02

*The average XPS oxidation state of Pt is calculated using the following equation: Pt (average oxidation state) = (mole fraction Pt(IV) × 4) + (mole fraction Pt(II) × 2) + (mole fraction Pt(0) × 0), where the mole fraction equals the XPS fraction % / 100 and these values are given in Figure 6. The final oxidation state values are rounded to two decimal places.

S.2.3.2. Fe 2p-XPS spectra

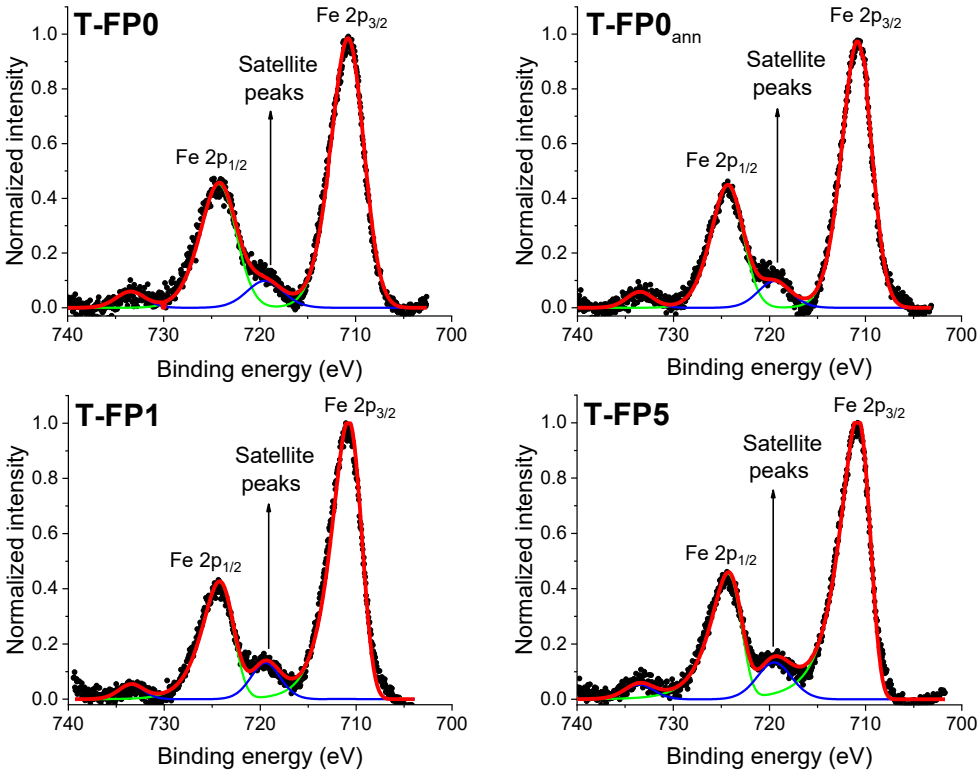

Figure S7. Fe 2p-XPS spectra of synthesized samples.

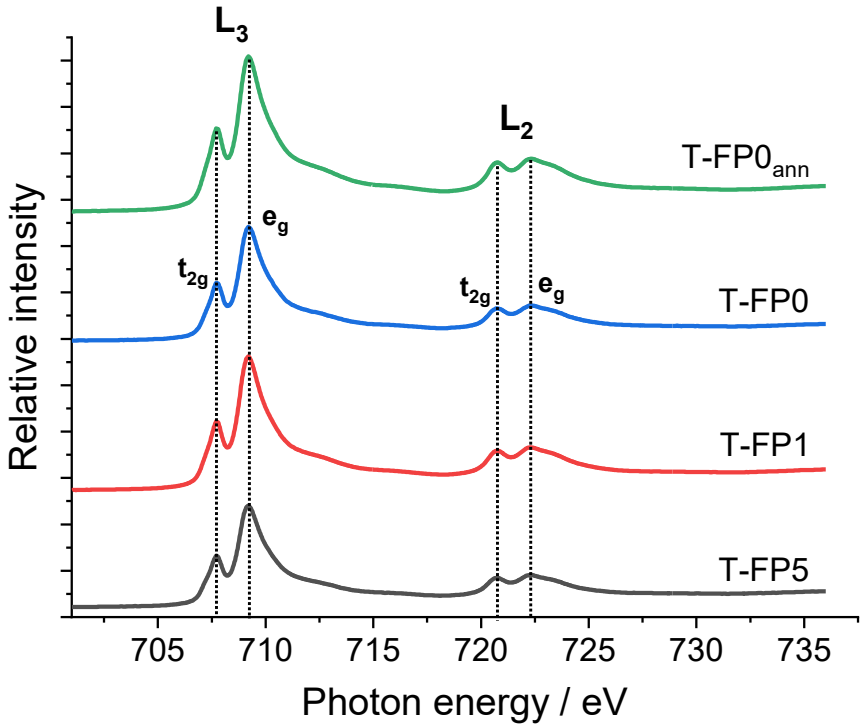

Figure S8. Fe $L_{2,3}$ edge NEXAFS spectra of T-FP0, T-FP0$_{ann}$, T-FP1 and T-FP5. The L_3 region occurs at ~707–709 eV (Fe $2p_{3/2} \rightarrow 3d$ transitions), while L_2 region occurs at ~720–722 eV (Fe $2p_{1/2} \rightarrow 3d$ transitions). The multiplet structures within the L_3 edge are attributed to transitions into the t_{2g} and e_g states characteristic of Fe^{3+} in α-Fe_2O_3. The similarity of the spectra confirms the preservation of the hematite electronic structure after Pt decoration and annealing.

S.2.3.3. O 1s-XPS spectra

The peak at ~531 eV (gray, Fig. 5) includes minor contributions from phosphate (Table S1), carbonate, and organic residues. The peaks at ~532 and ~533 eV correspond to surface hydroxyl groups (–OH) and adsorbed water, respectively. Both are more intense in Pt-decorated samples, indicating enhanced adsorption of oxygen-containing species due to strong Pt–O interactions.[8–15] In contrast, the annealed hematite (T-FP0$_{ann}$) shows a reduced ~532 eV peak and no signal at ~533 eV, suggesting that thermal treatment effectively removes surface –OH and H_2O. A weak peak at ~528 eV, observed in Pt-decorated samples, is attributed to subsurface oxygen species; its increased intensity with Pt content reflects stronger oxygen adsorption associated with oxidized Pt species (Pt^{2+}/Pt^{4+}).[12,13]

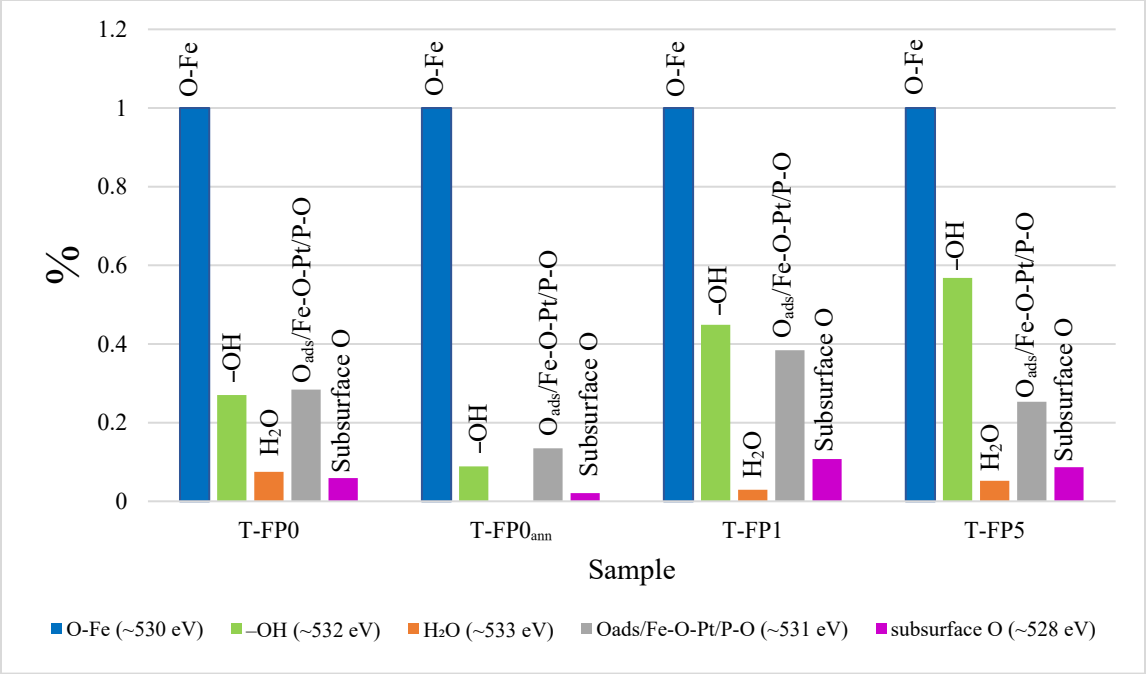

Figure S9. Quantitative distribution of oxygen species (%) in the synthesized samples T-FP0, T-FP0$_{ann}$, T-FP1 and T-FP5, determined by numerical fitting of high-resolution O 1s XPS spectra. The intensities of all components are normalized to the O–Fe peak in each sample to allow a comparative assessment of the oxygen species at the surface.

S2.4. TGA/DTG/DSC results

Figure S10 shows the thermogravimetric (TGA) curve of the hematite sample (T-FP0) recorded between 35 and 1000°C. The analysis reveals three main stages of mass loss. The first mass loss (≈ 0.62 wt%) observed below 200°C is attributed to the removal of physically adsorbed and weakly hydrogen-bonded water from the surface of the hematite nanotubes. The second mass loss (≈ 0.34 wt%) occurring between 200 and 400°C is associated with the dehydration of chemisorbed water, dehydroxylation of surface Fe-OH groups, and initial dehydration of hydrated, chemisorbed phosphate species introduced during hydrothermal synthesis. Notably, phosphate species do not desorb from the surface in this temperature range but undergo progressive dehydration and structural reorganization, leading to stronger Fe-O-P bonding. The most pronounced mass loss (≈ 1.30 wt%) occurs between 400 and 650°C and is attributed to dehydroxylation of strongly bound surface hydroxyl groups and condensation and dehydration of chemisorbed phosphate species, resulting in irreversible surface reconstruction through the formation of Fe-O-Fe and Fe-O-P linkages. This process reflects thermally activated surface densification rather than any bulk phase transformation, as α-Fe_2O_3 is already the thermodynamically stable iron oxide phase. At temperatures above 700°C, no further significant mass loss is observed. A slight mass increase may occur, which can be attributed to surface reoxidation of oxygen-deficient sites or limited oxygen uptake under ambient atmosphere. Although oxygen adsorption is generally less favorable at elevated temperatures, chemisorption at defect sites and surface re-equilibration can still occur.

The thermal behavior is consistent with literature reports on hydrothermally synthesized iron oxide nanostructures and confirms that the annealing temperature of 380°C (used for the T-FP0$_{ann}$ sample) is sufficient to ensure phase stability and substantial removal of surface-bound water and labile hydroxyl species, while preserving the α-Fe_2O_3 structure.[16–18]

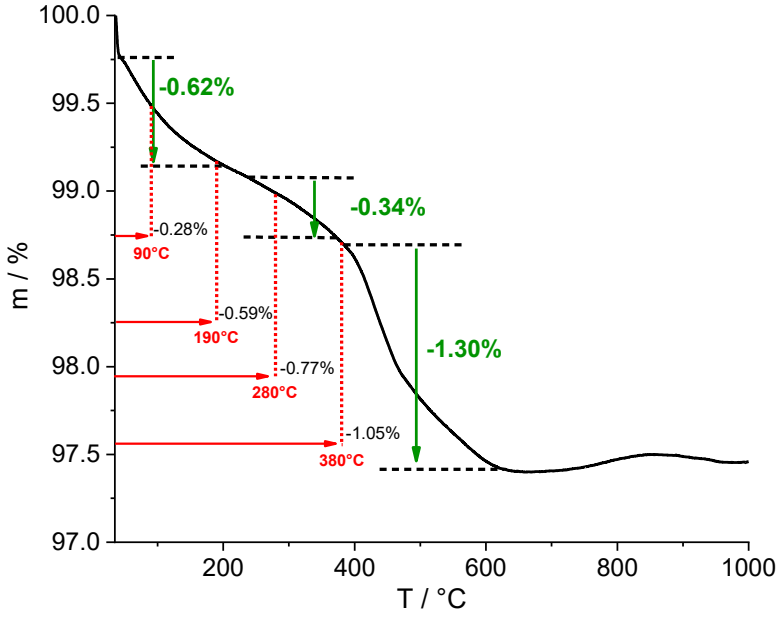

Figure S10. TGA thermogram of the T-FP0 sample showing percentage weight change as a function of temperature. The additional temperatures correspond to the gas sensing measurements (90°C, 190°C and 280°C) and the annealing process (380°C).

Figure S11 shows the combined TGA (black), DTG (blue), and DSC (red) curves for the T-FP0 sample. The initial mass loss observed below 100°C is attributed to the removal of physisorbed and weakly hydrogen-bonded water adsorbed on the surface of the hematite nanotubes. This process is accompanied by a broad DTG feature and a weak endothermic DSC signal, consistent with physical desorption processes typical of high-surface-area oxide nanostructures. In the intermediate temperature range (~200–350°C), a further gradual mass loss is detected, assigned to the dehydroxylation of surface Fe–OH groups and partial dehydration of hydrated phosphate species chemisorbed on the α-Fe_2O_3 surface. The broad DTG signal in this region indicates a distribution of surface binding energies, reflecting the heterogeneous chemical environments present on the inner and outer surfaces of the nanotubular architecture. A pronounced endothermic DSC/DTA event occurs between ~390 and 475°C, coinciding with the largest mass-loss step (~1.3 wt%) and a well-defined DTG minimum. This process is attributed to the dehydroxylation of strongly bound surface hydroxyl groups and the condensation and dehydration of chemisorbed phosphate species, leading to irreversible surface reconstruction. These transformations involve the formation of more stable Fe–O–Fe and Fe–O–P linkages through condensation reactions,

accompanied by the release of structural water. Notably, the endothermic signal extends with significantly reduced intensity up to approximately 600°C, suggesting the gradual completion of dehydroxylation and phosphate condensation processes associated with more strongly coordinated surface species and subsurface hydroxyls. This extended tail indicates a kinetically slow, thermally activated surface reorganization rather than a discrete phase transition. Importantly, no evidence of bulk phase transformation is observed, confirming that the α-Fe_2O_3 crystal structure remains thermally stable throughout this temperature range. At temperatures above ~800°C, a weak and broad exothermic drift is observed in the DSC signal, attributed to grain growth, sintering, and further crystallization of α-Fe_2O_3, leading to structural densification without significant mass loss.

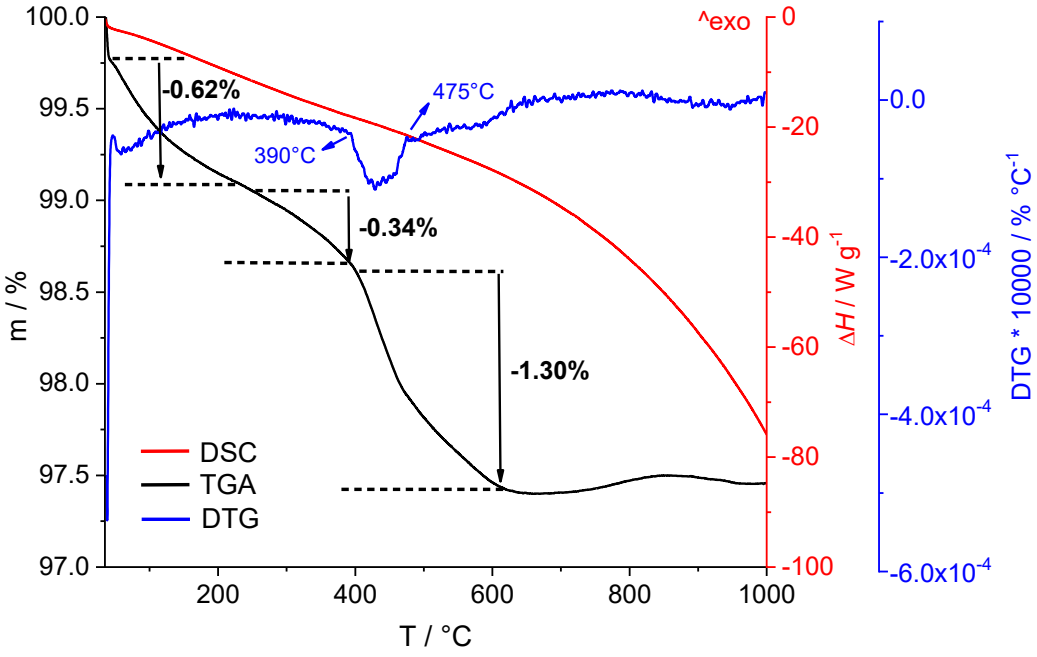

Figure S11. Combined TGA–DTG–DSC diagram of sample T-FP0, with the DSC curve in red, the TGA curve in black, and the DTG curve in blue, showing the mass loss steps and corresponding thermal events.

S2.5. Mössbauer spectroscopy results

Iron microenvironments were investigated using ^{57}Fe Mössbauer spectroscopy in Pt-free hematite nanotubes (T-FP0) and in hematite nanotubes decorated with 1 mol% (T-FP1) and 5 mol% Pt (T-FP5). Figure S12 shows the room temperature ^{57}Fe Mössbauer spectra of samples T-FP0, T-FP1, and T-FP5. The spectra display a sextet profile, characteristic of bulk hematite.[19] However, inward shoulders are observed on the individual absorption peaks, making them slightly asymmetric. These shoulders indicate the presence of minor sextet components with hyperfine magnetic fields lower than that of the main spectral component. This effect on the peak profiles is

similar to what would be expected in the presence of collective magnetic excitations. To estimate the effective volume of the nanotubes, we approximate their size as 70 nm outer diameter, 30 nm inner diameter, and 200 nm length. The volume of a tube of this size is equivalent to that of a sphere with a diameter of ca. 100 nm. However, significant magnetic relaxation effects in hematite are expected only at smaller particle sizes.[20] Therefore, we interpret the components with reduced hyperfine magnetic field values as hematite exhibiting structural deviations from the ideal crystal structure. These deviations may result from structural hydroxide groups and water molecules entrapped in the hematite structure during preparation, which were also hypothesized to be present based on TGA results (Fig. S10).[21] Accordingly, we fitted the spectra with several sextet components characterized by decreasing mean hyperfine magnetic field values and a Gaussian distribution of hyperfine magnetic fields with different standard deviations. The latter was modeled using Voigt based fitting[6] as implemented in the MossWinn program, without assuming distributions in the isomer shift and quadrupole shift parameter values. Four sextets (labeled A, B, C and D in Fig. S12) were necessary to achieve an acceptable fit of the spectra.

The room temperature Mössbauer spectra of samples T-FP0, T-FP1 and T-FP5 (Fig. S12) show only minor differences. To identify the main cause of these differences we assumed that the spectra could be composed of the same four sextet subcomponents, with possible differences in their relative spectral areas across the spectra. The Lorentzian contribution to the peak widths of the individual sextets was assumed to be the same, as was the relative area fraction of the 2nd and 5th peaks compared to that of the 3rd and 4th peaks of the sextets. This constrained model produced the fits shown in Fig. S12 and the associated Mössbauer parameters listed in Table S4. Sextet A, which dominates all three spectra, exhibits parameters closest to those ($\delta \approx 0.37$ mm/s, $2\varepsilon \approx -0.21$ mm/s, $B_{hf} \approx 51.7$ T) characteristic of bulk hematite.[19] In comparison, the subsequent components B, C and D display gradually decreasing relative area fractions and mean hyperfine magnetic fields, increasing standard deviations of the hyperfine magnetic field distribution, and overall larger deviations from the ideal Mössbauer parameters of bulk hematite. Based on Table S4, the main differences between the spectrum of sample T-FP0 and those of samples T-FP1 and T-FP5 are the larger relative area fraction of Sextet A and the lower relative area fraction of Sextet B (and to a lesser extent, Sextet C) in the latter. This is also clearly visualized in the cumulative hyperfine magnetic field distribution functions for the three samples shown in Fig. S13. These differences can be interpreted as the transformation of hematite 'B' structures into hematite 'A' structures, and to a lesser extent, hematite 'C' structures into 'B' and/or 'A' structures, as a result of the heat treatment used to prepare samples T-FP1 and T-FP5 from T-FP0. Since heat treatment is expected to reduce the concentration of structurally bound water and hydroxyl groups, as well as residual phosphate ions in hematite, the A, B, C, and D subcomponents may correspond-in this order-to increasing concentrations of hydration-related and possibly phosphate residual species in the hematite structure.

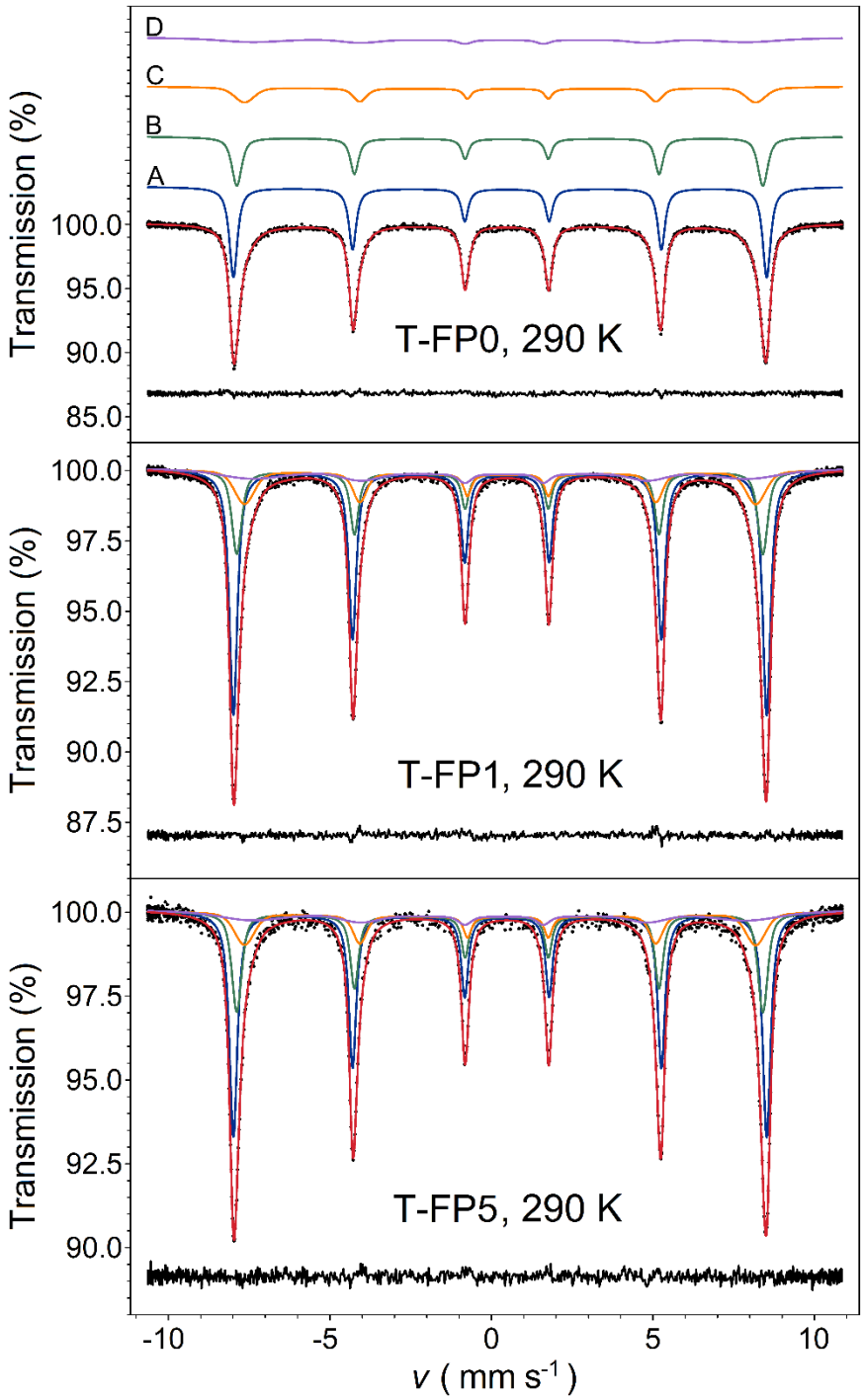

Figure S12. Room temperature ^{57}Fe Mössbauer spectra (black dots) of samples T-FP0, T-FP1 and T-FP5, along with their decomposition and fit envelope (solid lines). The respective fit residuals are displayed below the spectra. For T-FP0, the subcomponents are shifted upward for clarity. See Table S4 for the Mössbauer parameters associated with the subcomponents labeled A, B, C and D.

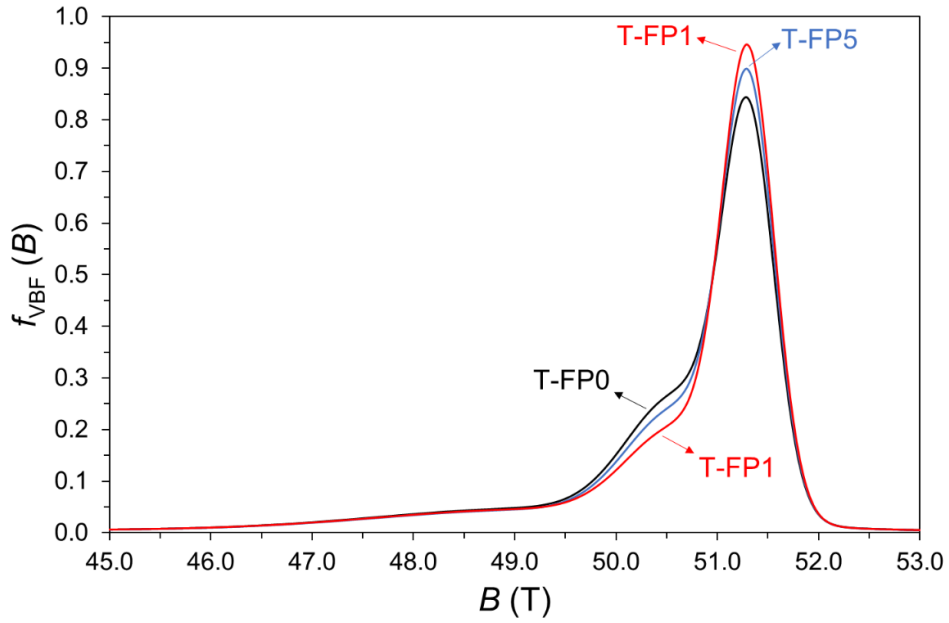

Figure S13. Hyperfine magnetic field distributions in the samples T-FP0, T-FP1 and T-FP5 as derived from the room temperature ^{57}Fe Mössbauer spectra shown in Fig. S12. The distributions shown are the cumulative hyperfine magnetic field probability density functions (f_{VBF}, where VBF refers to Voigt based fitting) of the individual subcomponents presented in Fig. S12. See Table S4 for the associated fit parameter values.

Table S4. Room temperature ^{57}Fe Mössbauer parameters of hematite nanotube samples T-FP0, T-FP1 and T-FP5 obtained from the simultaneous fit of the spectra shown in Fig. S12. Numbers in parentheses indicate the statistical error (1σ) in the last digit.*

Sample	T-FP0	T-FP1	T-FP5
χ^2_n	1.22	1.24	1.11
Hematite (A)			
RA, %	46.8(2)	55.0(2)	51.0(3)
A_{25}/A_{34}	1.943(3)		
δ, mm s^{-1}	0.3747(4)		
$\langle B_{hf} \rangle$, T	51.306(5)		
2ε, mm s^{-1}	-0.214(1)		
$\sigma(B_{hf})$, T	0.256(7)		
W_L, mm s^{-1}	0.262(1)		

Hematite (B)			
RA, %	29.3(2)	21.8(1)	26.3(3)
A_{25}/A_{34}	1.943(3)		
δ, mm s^{-1}	0.368(1)		
$\langle B_{hf} \rangle$, T	50.61(1)		
2ε, mm s^{-1}	-0.214(2)		
$\sigma(B_{hf})$, T	0.50(2)		
W_L, mm s^{-1}	0.262(1)		
Hematite (C)			
RA, %	15.5(2)	14.7(2)	14.5(3)
A_{25}/A_{34}	1.943(3)		
δ, mm s^{-1}	0.391(3)		
$\langle B_{hf} \rangle$, T	49.19(3)		
2ε, mm s^{-1}	-0.240(6)		
$\sigma(B_{hf})$, T	1.51(4)		
W_L, mm s^{-1}	0.262(1)		
Hematite (D)			
RA, %	8.4(2)	8.5(2)	8.2(4)
A_{25}/A_{34}	1.943(3)		
δ, mm s^{-1}	0.32(2)		
$\langle B_{hf} \rangle$, T	47.7(2)		
2ε, mm s^{-1}	-0.14(3)		
$\sigma(B_{hf})$, T	5.1(2)		
W_L, mm s^{-1}	0.262(1)		

*χ^2_n is the normalized chi-square of the fit, RA denotes the relative spectral area, A_{25}/A_{34} is the relative area of the 2nd and 5th peaks of the sextet components wrt. that of the 3rd and 4th peaks, δ denotes the isomer shift relative to α-Fe at room temperature, $\langle B_{hf} \rangle$ is the mean and $\sigma(B_{hf})$ is the standard deviation of the Gaussian hyperfine magnetic field distribution associated with the corresponding component, ε is the first order quadrupole shift, W_L is the Lorentzian FWHM line width contribution to the apparent peak width of the sextet components.

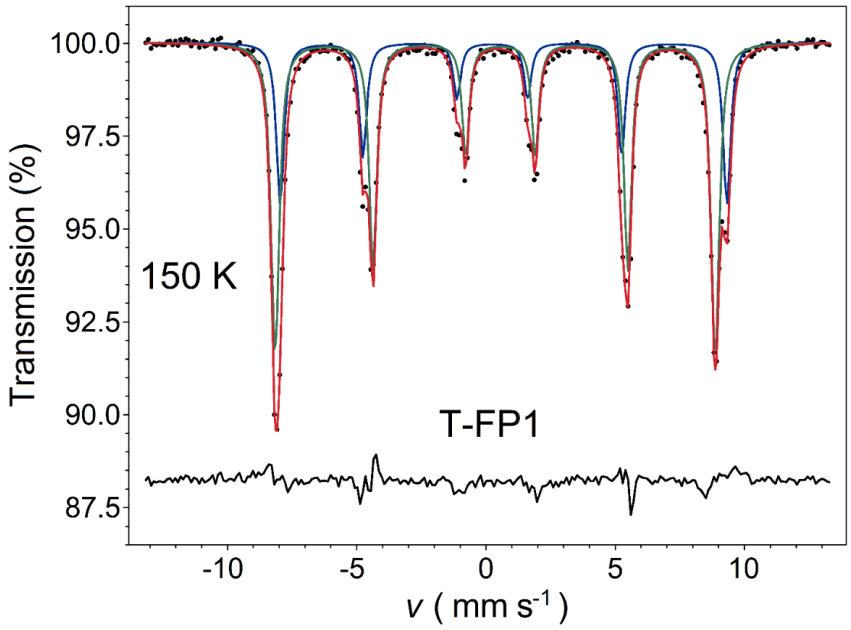

Figure S14. ^{57}Fe Mössbauer spectrum (black dots) of sample T-FP1 recorded at 150 K, along with its decomposition and fit envelope (solid lines). The fit residual is shown below the spectrum. See Table S5 for the corresponding Mössbauer parameters.

Table S5. ^{57}Fe Mössbauer parameters of the hematite nanotube sample T-FP1 at 150 K. See Fig. S14 for the corresponding Mössbauer spectrum. Numbers in parentheses indicate the statistical error (1σ) in the last digit. The Lorentzian FWHM line width (W_L) was fixed to its value found at 87 K. See Table S4 for further notations.

Sample	T-FP1
T, K	150
χ^2_n	5.91
S1 (Hematite without Morin transition)	
RA, %	66.8(3)
A_{25}/A_{34}	2.04(1)
δ, mm s^{-1}	0.457(1)
$\langle B_{hf} \rangle$, T	52.913(6)
2ε, mm s^{-1}	-0.204(2)

$\sigma(B_{hf})$, T	0.43(1)
W_L, mm s^{-1}	0.319(F)
S2 (Hematite with Morin transition)	
RA, %	33.2(3)
A_{25}/A_{34}	2.04(1)
δ, mm s^{-1}	0.462(2)
$\langle B_{hf} \rangle$, T	53.70(1)
2ε, mm s^{-1}	0.435(3)
$\sigma(B_{hf})$, T	0.33(3)
W_L, mm s^{-1}	0.319(F)

While the Mössbauer spectra of samples T-FP0, T-FP1 and T-FP5 showed only minor differences at room temperature, low temperature measurements (Fig. S15) performed at T = 87-88 K revealed marked differences between the samples. The spectrum of T-FP0 at 87 K consists of a single sextet component, whereas those of T-FP1 and T-FP5 exhibit two well-defined subcomponents. Based on the Mössbauer parameters (Table S6), the sextet component observed for T-FP0 is anomalous. Hematite is known to undergo a magnetic transition when cooled below its Morin transition temperature, $T_M \approx$ 250-260 K, leading to a reorientation of the iron magnetic moments from perpendicular ($T > T_M$) to parallel ($T < T_M$) to the c-axis of the hexagonal lattice. Thus, below ~ 250 K, a perfect antiferromagnetic (AF) structure is observed, while above ~ 250 K, a canted antiferromagnetic structure results, which manifests as a weak ferromagnet (WF).[19,22–24] In the Mössbauer spectrum, this transition is detectable as a change in the sign of the ε quadrupole shift, resulting in a change of 2ε from $2\varepsilon \approx -0.2$ mm/s ($T > T_M$) to $2\varepsilon \approx 0.4$ mm/s ($T < T_M$).[21,24–26] Another characteristic of the transition is that the ^{57}Fe hyperfine magnetic field is ca. 0.8 T higher in the purely antiferromagnetic state ($T < T_M$) than in the weakly ferromagnetic one ($T > T_M$).[23] Considering the above and the results listed in Table S6, it follows that sample T-FP0 did not undergo the Morin transition within the temperature range of 87 K to 290 K. Instead, its Mössbauer spectrum (Fig. S15) reflects a negative quadrupole shift value with $2\varepsilon \approx -0.20$ mm/s (Table S6) which is characteristic of the weakly ferromagnetic ($T > T_M$) state of hematite. Several factors could explain the absence of the Morin transition. Strains, crystal defects, impurities and surface effects are known to reduce the Morin temperature.[27,28] Additionally, for particles smaller than ca. 100 nm, the Morin transition temperature decreases rapidly with decreasing particle size, disappearing entirely for nanoparticles smaller than 10 nm.[27,29] For larger particles, the incorporation of structural hydroxyls and molecular water into the hematite structure, along with the resulting changes in lattice parameters, may play a decisive role in suppressing the Morin

transition.[21] For the present samples, this scenario aligns with the analysis results from the room-temperature Mössbauer spectra (Fig. S12) and the TGA measurement (Fig. S10).

The two sextet components revealed by the Mössbauer spectra of hematite nanotubes decorated with platinum are clearly distinguished by their Mössbauer parameters (Table S6). The first sextet S1, exhibited parameter values closely resembling those of the T-FP0 hematite nanotubes, indicating that a portion of the material retained its original structural and magnetic properties. In contrast, the second sextet, S2, displayed parameter values ($2\varepsilon \approx 0.43$ mm/s and a mean hyperfine magnetic field that is ca. 0.8 T higher than that of the corresponding S1 component) characteristic of hematite that had undergone the Morin transition. The relative spectral area of S2 was ~34% in the case of T-FP1 and ~29% in the case of T-FP5, i.e. the applied heat treatments (Table 1) recovered the Morin transition in a substantial part of these samples.

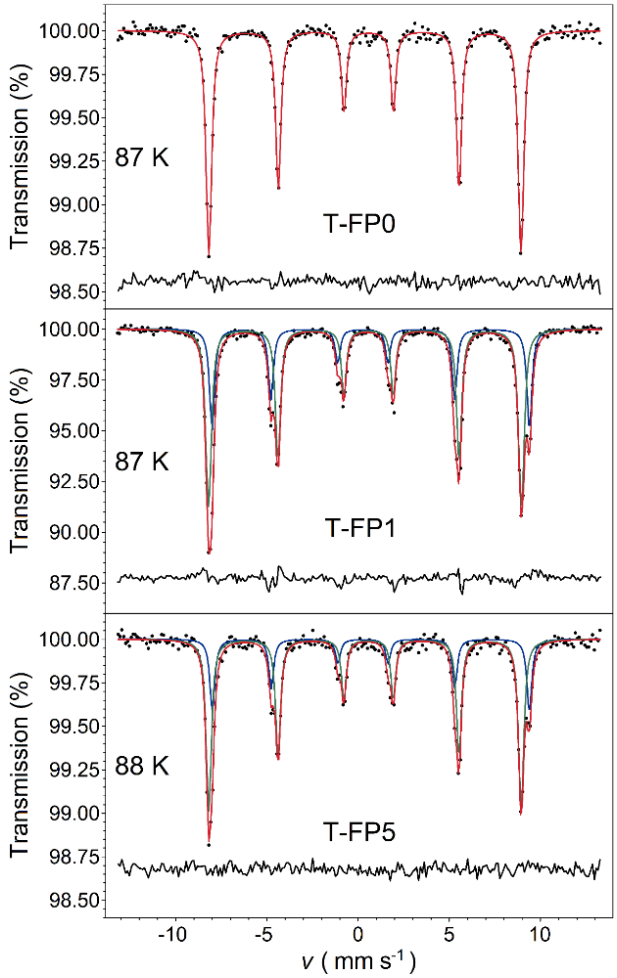

Figure S15. ^{57}Fe Mössbauer spectra of samples T-FP0, T-FP1 and T-FP5 recorded at the indicated temperatures, along with their decomposition and fit envelope. The respective fit residuals are displayed below the spectra.

Table S6. Low temperature (T = 87-88 K) ^{57}Fe Mössbauer parameters of hematite nanotubes with and without platinum decoration. Numbers in parentheses indicate the statistical error (1σ) in the last digit.*

Sample	T-FP0	T-FP1	T-FP5
T, K	87	87	88
χ^2_n	1.04	3.20	1.00
S1 (Hematite without Morin transition)			
RA, %	100.00	66.2(4)	71.1(1.1)
A_{25}/A_{34}	2.00(3)	2.05(1)	1.98(3)
δ, mm s^{-1}	0.479(2)	0.478(1)	0.476(2)
$\langle B_{hf} \rangle$, T	53.22(1)	53.34(1)	53.26(2)
2ε, mm s^{-1}	-0.202(3)	-0.196(3)	-0.196(5)
$\sigma(B_{hf})$, T	0.38(3)	0.43(2)	0.27(6)
W_L, mm s^{-1}	0.319(4)		
S2 (Hematite with Morin transition)			
RA, %		33.8(4)	28.9(1.1)
A_{25}/A_{34}		2.05(1)	1.98(3)
δ, mm s^{-1}		0.478(2)	0.486(6)
$\langle B_{hf} \rangle$, T		54.10(1)	54.04(4)
2ε, mm s^{-1}		0.436(4)	0.43(1)
$\sigma(B_{hf})$, T		0.18(7)	0.0(1)
W_L, mm s^{-1}		0.319(4)	

*χ^2_n is the normalized chi-square of the fit, RA denotes the relative spectral area, A_{25}/A_{34} is the relative area of the 2nd and 5th peaks of the associated magnetic sextet component wrt. that of the 3rd and 4th peaks, δ denotes the isomer shift relative to α-Fe at room temperature, $\langle B_{hf} \rangle$ is the mean and $\sigma(B_{hf})$ is the standard deviation of the Gaussian hyperfine magnetic field distribution associated with the corresponding component, ε is the first order quadrupole shift, W_L is the Lorentzian FWHM line width contribution to the apparent peak width of the sextet components. The latter was constrained to be equal for all subcomponents of the fit.

To confirm that the relative area fractions determined for the S2 component in samples T-FP1 and T-FP5 accurately represent the proportion of iron microenvironments in hematite that underwent the Morin transition, T-FP1 was also measured at 150 K. Decomposition of the T-FP1 spectrum at 150 K (Fig. S14) yields parameter values (Table S5) consistent with those found at 87 K (Table S6), with component S2 exhibiting nearly the same relative area fraction at both temperatures. This result demonstrates that the temperature dependence of the iron recoilless fractions associated with components S1 and S2 does not differ appreciably. It also indicates that the microenvironments associated with S2 do not gradually emerge from those of component S1 as the temperature decreases. Instead, they exist as distinct, well-defined microenvironments with a specific concentration within the structure of the hematite nanotubes. In Table S6, the standard

deviation $\sigma(B_{hf})$ of the hyperfine magnetic field distribution for component S2 is significantly smaller than the corresponding value for component S1 in both, T-FP1 and T-FP5. This further suggests that S2 is associated with a microenvironment having a distinct structure with low variability, which can presumably be identified as the ideal hematite structure. In contrast, microenvironments resulting in component S1 can be characterized by high variability, likely related to the distribution of residual molecular water, hydroxyl groups, and phosphate ions in the hematite structure.

S2.6. EPR spectroscopy results

X-band electron paramagnetic resonance spectroscopy measurements were conducted to monitor the effects of heat treatment (Table 1) and the occurrence of the Morin transition through changes in the EPR signal in the temperature range of 150-290 K. Figure S16 compares X-band EPR spectra of samples T-FP0, T-FP1 and T-FP5 at 290 K and 150 K (See Fig. S17 for a more detailed temperature dependence of the EPR signal). Based on spectra recorded at 290 K, the heat treatment applied for Pt decoration resulted in the enhancement of a broad signal extending from 100 G to above 5000 G. This enhancement makes the room temperature spectra of T-FP1 and T-FP5 distinctly different from that of T-FP0. However, when the samples are cooled to 150 K, the spectra of the three samples become more similar (Fig. S16).

Among the possible electron magnetic resonance modes of hematite, in the X-band (microwave wavelength $\lambda \approx 3$ cm) the low-frequency mode of the weak ferromagnetic state (mode LFWF) is expected to be observable in the EPR spectra.[30,31] This mode involves the precession of the weak ferromagnetic moment of hematite (for $T > T_M$) around the applied magnetic field. Due to zero field splitting, the center of the associated LFWF electron magnetic resonance signal is expected to appear around $B = 0$ G for microwave frequencies in the X-band.[31,32] Furthermore, as the temperature decreases, the microwave absorption associated with the LFWF mode reduces to zero once the Morin transition is completed.[31–33]

The first integral of the EPR signals shown in Fig. S16 provides the magnetic field dependence of microwave absorption, as presented in Fig. S18. In this case, these dependencies indicate that the hypothetical center of the microwave absorption band is indeed near, and slightly below, zero applied magnetic field. The decrease in absorption in this band as the temperature is lowered from 290 K to 150 K also supports attributing the enhanced EPR signal observed for the T-FP1 and T-FP5 samples to the LFWF resonance signal theoretically expected for the ideal hematite structure. This signal can be considered characteristic of the portion of the T-FP1 and T-FP5 samples that undergoes the Morin transition, as indicated by the respective Mössbauer spectra (Fig. S18). The deviation of the EPR spectra of T-FP1 and T-FP5 from that of T-FP0 at 290 K, i.e. in the weakly ferromagnetic state, indicates that *even at room temperature* the magnetic properties of the original hematite structure characteristic of T-FP0 differ considerably from those of the closer-to-ideal hematite structure formed in its heat treated and Pt decorated counterparts. This difference is presumably due to changes in local magnetic anisotropies as heat treatment reduces the concentration of phosphate (PO_4^{3-}) and hydration-related residual species in the samples.

It has been shown that hematite nanoparticles undergoing superparamagnetic relaxation contribute to the EPR spectrum with a broad absorption band at around $g = 2$.[31] The absence of a corresponding absorption band with significant intensity in our samples (Figs. S16 and S18) rules out the notable presence of such superparamagnetic particles and further confirms the morphological consistency of the particles in these samples.

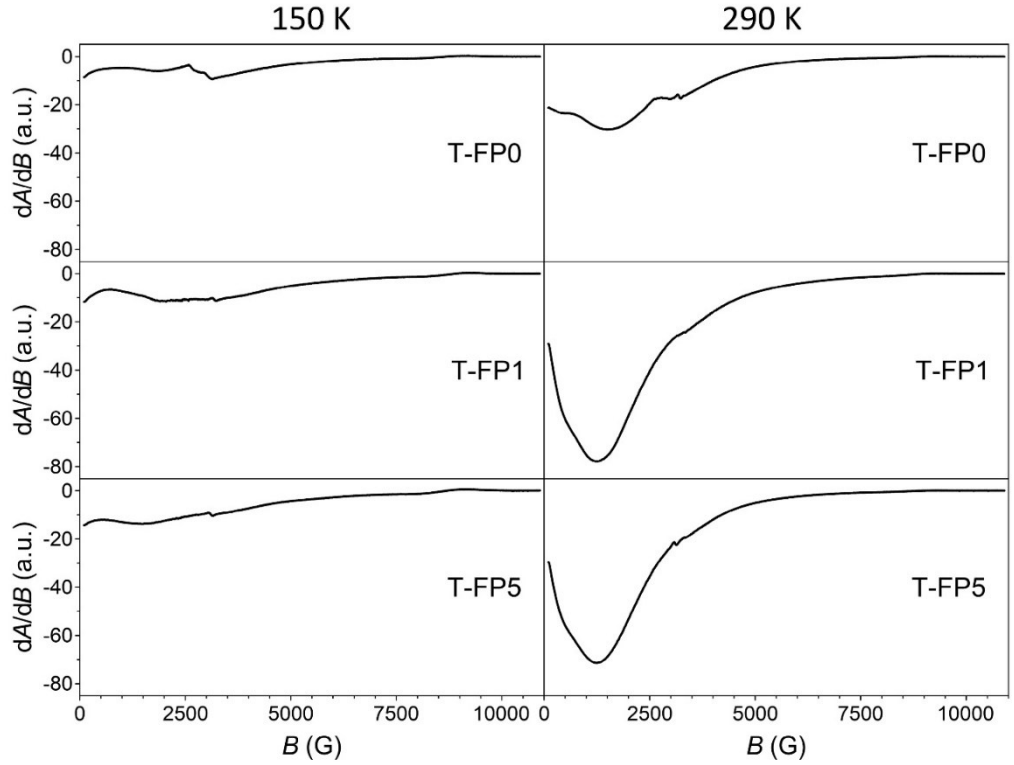

Figure S16. Comparison of the EPR spectra of T-FP0, T-FP1 and T-FP5 measured at 150 K and 290 K. Refer to Fig. S18 for the EPR spectra recorded between these two temperatures. Note that on the horizontal scale of these spectra $g = 2$ is equivalent to ~3326 G.

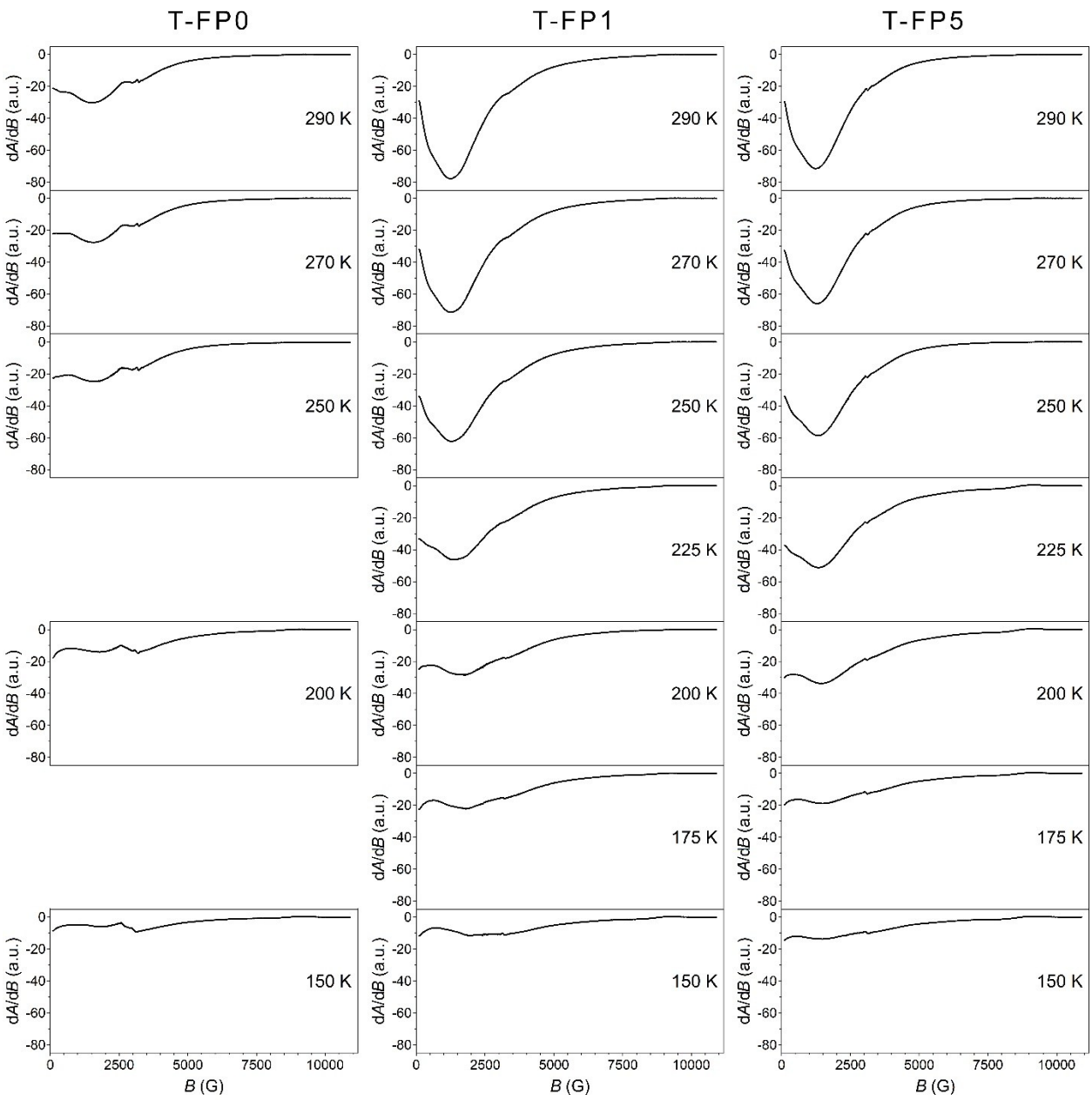

Figure S17. Temperature dependence of the X-band EPR spectra of the samples T-FP0, T-FP1 and T-FP5 recorded between 150 K and 290 K. T-FP0 was measured at only five different temperatures.

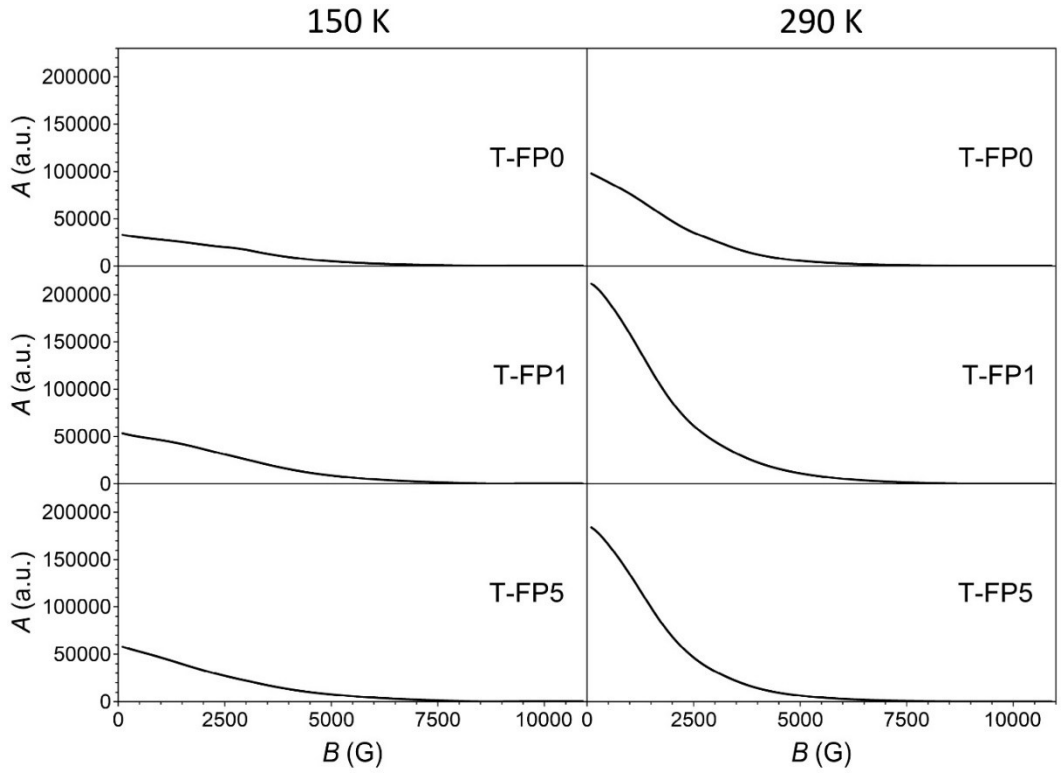

Figure S18. First integral of the respective EPR signals shown in Fig. 16, illustrating the magnetic field dependence of microwave absorption. The curves were vertically shifted so that the absorption minimum aligns with the zero level in each case.

S2.7. Results of magnetization measurements

A detailed analysis (Fig. 6) of the temperature-dependent magnetization (H = 100 Oe) reveals a bifurcation between the ZFC and FCC/FCW curves for all samples, which is typical of small magnetic particles. This separation becomes apparent near room temperature and results from the continuous freezing of magnetic moments aligned with the field during cooling (FCC/FCW), compared with the random freezing of moments in the absence of a field (ZFC). The ZFC curve (Fig. 6) for the samples in the measured temperature range shows no characteristic maximum at the blocking temperature, which usually separates the low-temperature blocked and high-temperature superparamagnetic regimes, i.e. magnetic moments remain blocked up to the highest measured temperatures. This indicates a relatively high anisotropy energy barrier, consistent with the sizes and elongated morphology of the hematite particles.

At high temperatures, all hematite samples have a canted antiferromagnetic spin structure giving rise to a net magnetic moment. Magnetic moment of antiferromagnetic nanoparticles can be further enhanced, compared to the bulk counterpart, due to structural disorder, broken bonds, and uncompensated interactions at the particle surface, which are more pronounced in smaller particles.

The ZFC and FCC curves of the T-FP0 sample (Fig. 6) do not show any indication of a marked Morin transition, consistent with the Mössbauer measurements. In contrast, the T-FP5 sample exhibits a pronounced Morin transition with significant thermal hysteresis, depending on whether the sample was measured during cooling ($T_M \approx 140$ K) or warming ($T_M \approx 180$ K). This observation also agrees with the Mössbauer measurements (Fig. 6). A lower T_M value and pronounced thermal hysteresis are typical for hematite particles with submicron sizes compared to bulk hematite.[27] Magnetization measurements of T-FP5 and T-FP0$_{ann}$ samples clearly show that only part of the samples underwent the Morin transition. The magnetization of a hematite sample in a perfect antiferromagnetic state at temperatures below the Morin transition and in a small applied magnetic field would be very small (practically zero). In contrast, the magnetization of our samples remains finite at the lowest temperatures, indicating that a weak ferromagnetic component is still present. Additionally, there is a splitting between the ZFC and FCC/FCW magnetization curves at the lowest temperatures consistent with the blocking of magnetic moments in particles with a weak ferromagnetic structure i.e. particles that did not undergo the Morin transition.

Figure 7 (a) shows the magnetic field dependence of the magnetization measured at T = 5 K, which does not differ significantly between the two samples. This behavior is consistent with an antiferromagnetic system containing a very small proportion of a ferromagnetic component, which could be due to weak ferromagnetism in hematite. The proportion of the ferromagnetic component appears significant only because the response to a magnetic field is much stronger in a ferromagnet than in an antiferromagnet. The linear increase in magnetization at high fields ($H \geq 20$ kOe) confirms that antiferromagnetism is the dominant magnetic interaction, while the low-field region exhibits a minor ferromagnetic-like contribution that saturates and gives rise to hysteresis, attributed to the slow relaxation of weakly ferromagnetic domains. Figure 7 (b) shows the temperature dependence of the real and imaginary components of magnetic ac susceptibility for the T-FP0$_{ann}$ sample. No clear traces of the Morin transition are observed, which is expected since antiferromagnets respond very poorly to an alternating magnetic field of small amplitude and only a small portion of the sample undergoes the Morin transition. The increase in both the real and imaginary components of ac susceptibility at higher temperatures can be attributed to the slow relaxation of magnetic moments, consistent with the DC magnetization shown in Fig. 6. The characteristic maximum of both parts of susceptibility, typical for single domain nanoparticle systems, is not achieved in the measured temperature range, implying a high anisotropy barrier.

For comparison, previously studied hematite nanoparticles provide insight into the thermal behavior and recovery of the Morin transition. The absence of the Morin transition in hematite synthesized from aqueous medium has been observed in ellipsoidal nanoparticles with mean major and minor axis sizes of 330 nm and 70 nm, respectively. Annealing these nanoparticles at temperatures up to ca. 500ºC did not restore the Morin transition; however, the transition was successfully recovered through heat treatments at higher temperatures.[34] In the present work, the maximum heat-treatment temperature used for the preparation of T-FP1 and T-FP5 was 380°C (Table 1), yet the Morin transition was successfully recovered in part of these samples (Table S6). The higher sensitivity of T-FP0 to heat treatments compared to the ellipsoidal nanoparticles studied previously could be due to morphological differences between these particles. Specifically, while

the characteristic size of T-FP0 particles (Figure 1) is roughly equal to that of the ellipsoidal particles mentioned above, the nanotube morphology of T-FP0 results in a higher surface-to-volume ratio, and therefore in a lower overall activation energy for the removal of hydroxyl groups and molecular water.[34]

S2.8. Hydrogen gas sensing properties

Table S7. Average baseline electrical resistance (R_0) of T-FP0, T-FP0$_{ann}$, T-FP1 and T-FP5 samples measured in air and nitrogen at 363, 463 and 553 K. Values represent the mean ± standard deviation (SD) of three repeated measurements.

Sample	R_0 / MΩ (air)			R_0 / MΩ (nitrogen)		
	363 K	463 K	553 K	363 K	463 K	553 K
T-FP0		19.0±2.2	2.82±0.4		93.9±7.8	22.2±7.9
T-FP0$_{ann}$		2.67±0.3	0.71±0.06		0.73±0.1	0.14±0.01
T-FP1	345±25.2	38.9±7.6	4.32±2.7	160±29.4	8.49±3.2	2.17±0.5
T-FP5	1200±433	188±54.4	18.7±9.7	640±176	197±11.8	38.9±8.1

S2.8.1. Effect of Pt decoration and temperature on hydrogen sensing in air

In air, oxygen molecules are adsorbed onto the α-Fe_2O_3 surface and capture electrons from the conduction band, forming surface oxygen species and an electron depletion layer. When exposed to H_2, the adsorbed oxygen reacts with hydrogen, releasing electrons back into the conduction band, which reduces the electron depletion width and decreases electrical resistance. In the presence of Pt nanoparticles, hydrogen dissociation and spillover processes enhance the reaction with adsorbed oxygen species, resulting in greater electron release and further narrowing of the depletion layer.[35–37] A schematic illustration of the proposed sensing mechanism is shown in Figure S19.

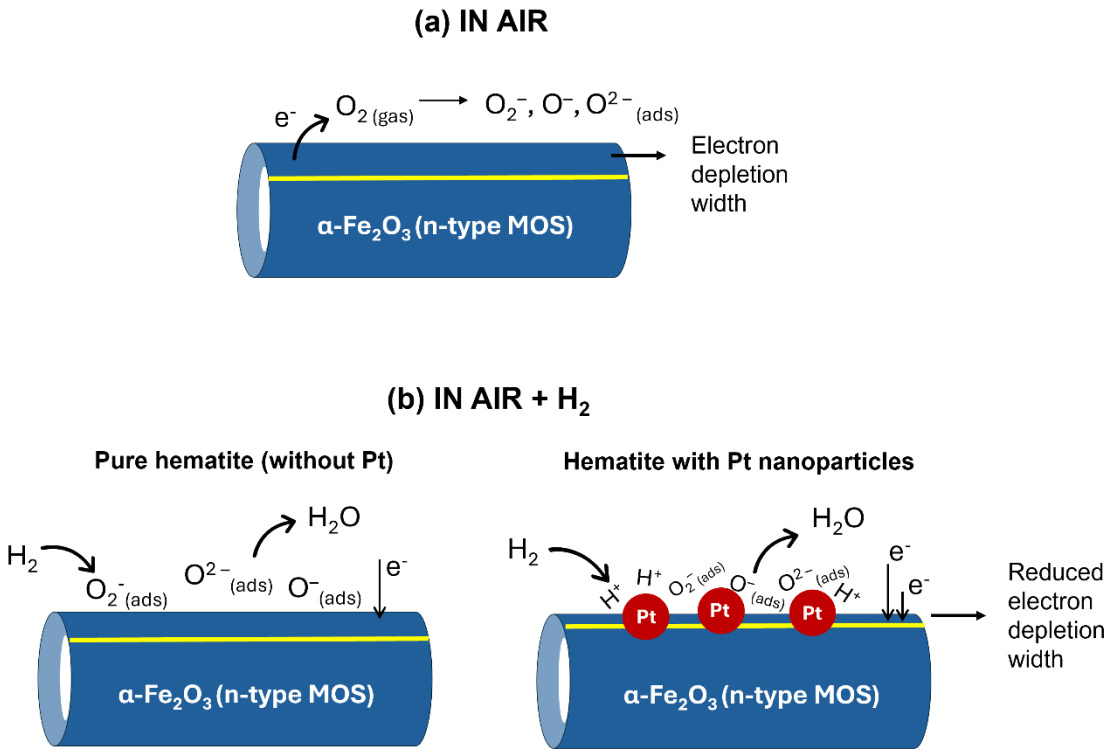

Figure S19. Schematic illustration of the proposed gas sensing mechanism for an n-type semiconducting metal oxide in air (a) and upon exposure to a reducing gas (hydrogen) (b), with and without Pt decoration. The electron depletion layer is widest in air due to oxygen adsorption, becomes thinner upon exposure to H_2 for pure hematite, and is further reduced in the presence of Pt nanoparticles because of enhanced hydrogen dissociation and spillover, resulting in the lowest electrical resistance.

Table S8. Comparative overview of hydrogen sensing performance reported for various metal-oxide semiconductor (MOS)–based hydrogen sensors.

Sensor	**Optimal working temperature (°C)**	**RH (%)**	**LOD (ppm H_2)**	**Concentration (ppm)**	**Response (R_{air}/R_{gas})**	**t_{res} (s)**	**Ref.**
Pt/Fe_2O_3 nanotubes	190	20–40	1	400	4.5	3.6	This work
$WO_{2.72}$ nanoparticles	RT	~ 35	NG	500	3.7	56	[36]
Ag/WO_3 thin film	RT	~ 0	NG	100	1.05	3	[38]
Pd/α-MoO_3 thin film	100	NG	800	NG	NG	287	[39]
TiO_2 mesoporous structured	RT	~ 0	100	1000	298	85	[40]
Pt/SnO_2 thin film	200	~ 0	NG	250	51.6	33.3	[41]
$Pd_1Ag_{0.50}$@SnO/ SnO_2 nanosheets	225	~ 0	NG	100	81.34	45	[42]
Pt/SnO_2-Co_3O_4 composite	300	NG	NG	100	45.1	12	[43]
Ir/ZnO	265	~ 50	NG	500	2.79	7@100 ppm	[44]

*RT denotes room temperature; RH denotes relative humidity and ~ 0% RH indicates dry conditions, i.e. measurements performed in dry air, without intentional introduction of humidity; t_{res} is the response time; LOD is the detection limit; NG indicates that the corresponding data were not provided in the cited references.

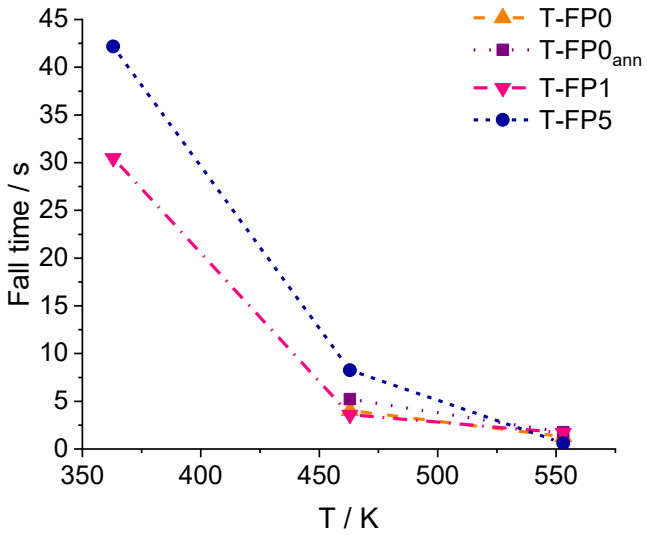

Figure S20. Average response time (fall time) of the electrical resistance for T-FP0, T-FP0$_{ann}$, T-FP1 and T-FP5 samples measured in air at different temperatures.

To further clarify the factors influencing hydrogen sensor performance, the effects of morphology and synthesis method were also examined. The results were compared with our previous study by Šoltić et al., in which hematite nanoparticles with irregular morphology synthesized by planetary ball milling were investigated (Figs. S21 and S22).[1] All measurements were performed using the same setup and identical experimental conditions to enable a direct comparison of the influence of both morphology and synthesis route on sensor behavior under oxidative conditions (air). It should also be noted that differences in synthesis approach (hydrothermal vs mechanochemical) may contribute to variations in crystallinity, defect density, and surface chemistry. The specific surface area of irregular hematite without Pt was 9.3 $m^2\ g^{-1}$, increasing to 14.9 $m^2\ g^{-1}$ with 1 mol% Pt decoration.[1] In contrast, nanotube samples exhibited considerably higher values: 24.4 $m^2\ g^{-1}$ for Pt-free nanotubes (T-FP0) and 36.5 $m^2\ g^{-1}$ for Pt-decorated nanotubes (T-FP1) (Fig. S23). These results confirm that both Pt decoration and controlled nanotube morphology substantially increase the available surface area, providing more active sites for gas interaction and improving overall sensor performance.

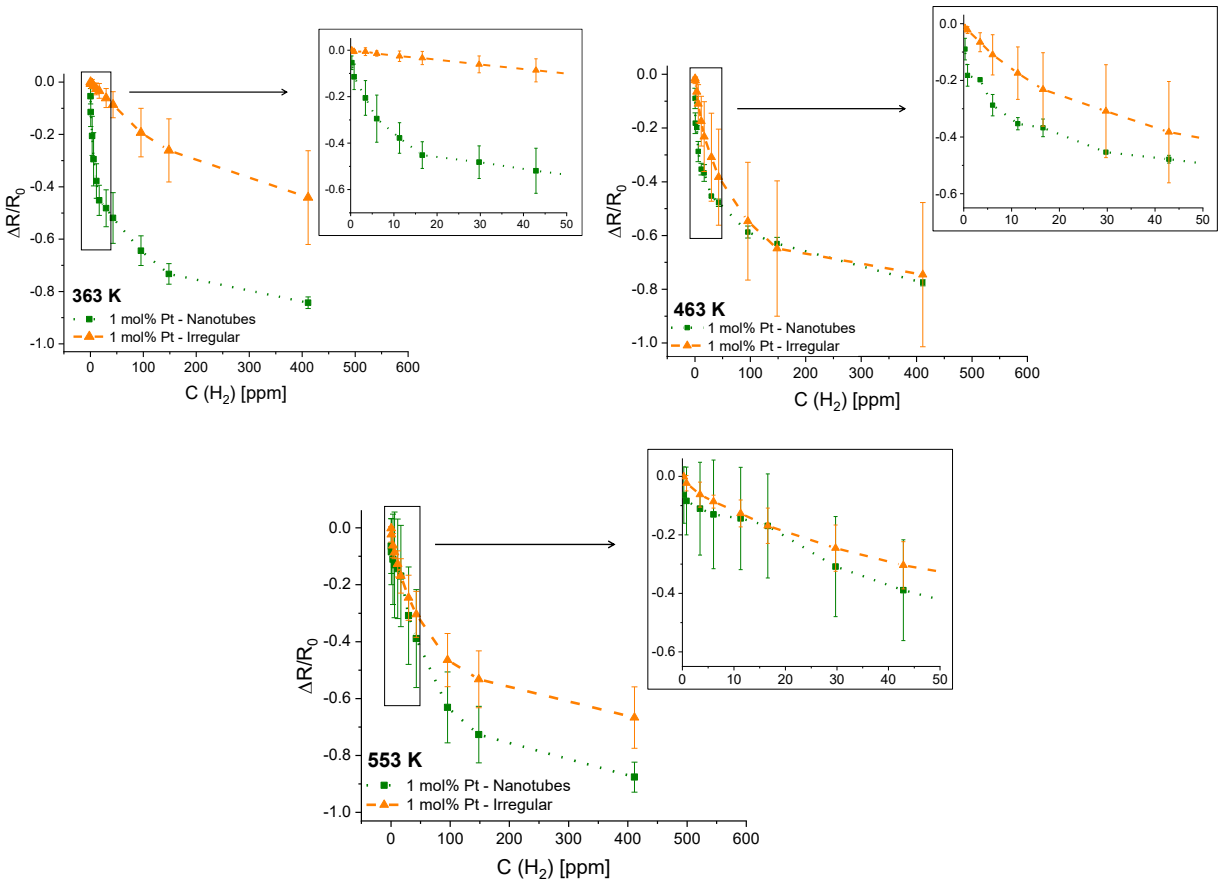

Figure S21. Comparison of 1 mol% Pt-decorated α-Fe_2O_3 samples with nanotubes (green square) and irregular morphology (orange triangle) from Šoltić et al.[1] The main plots show the entire concentration range, while the insets enlarge the range at low concentrations (0–50 ppm).

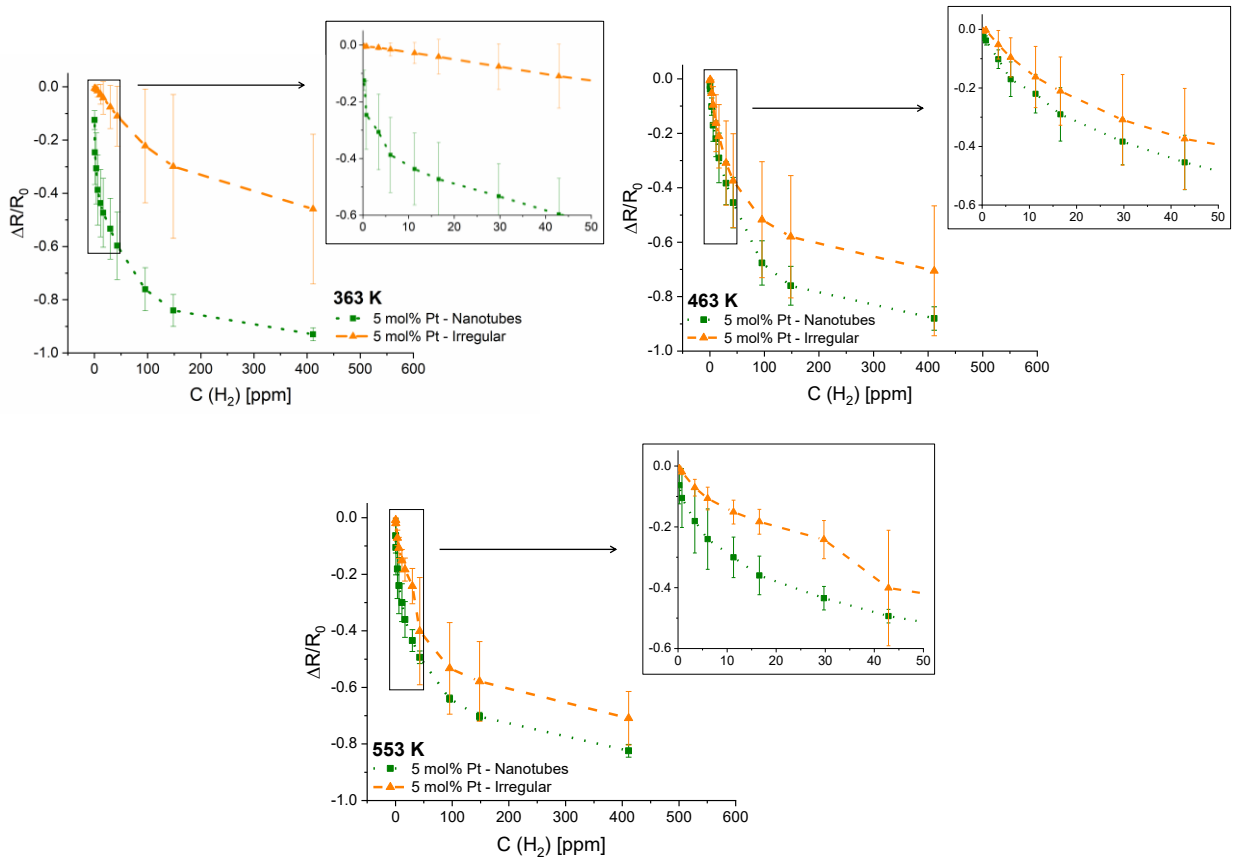

Figure S22. Comparison of 5 mol% Pt-decorated α-Fe_2O_3 samples with nanotubes (green square) and irregular morphology (orange triangle) from Šoltić et al.[1] The main plots show the entire concentration range, while the insets enlarge the range at low concentrations (0–50 ppm).

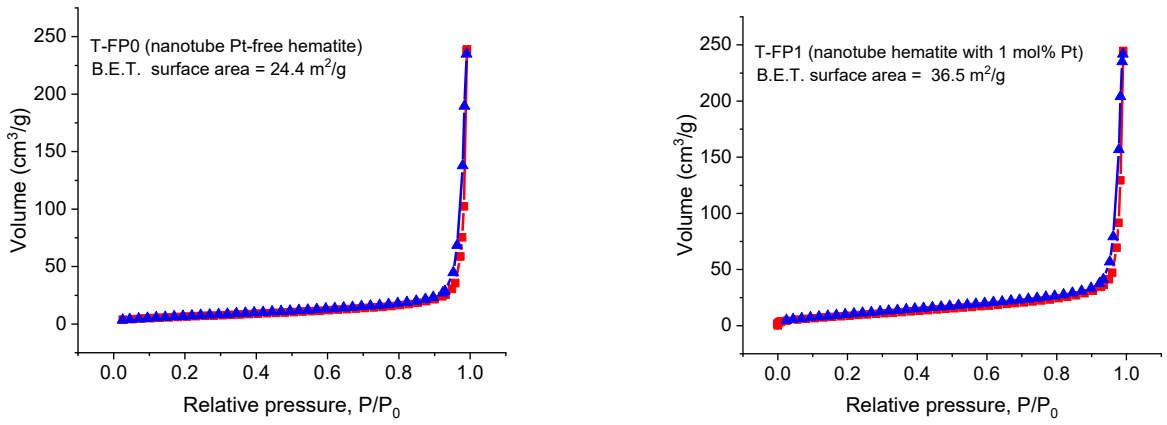

Figure S23. Gas (N_2) adsorption (red line, circles) and desorption (blue line, squares) isotherms and calculated BET surface areas of T-FP0 and T-FP1 samples.

S2.8.2. Influence of measurement atmosphere: comparison between air and N_2

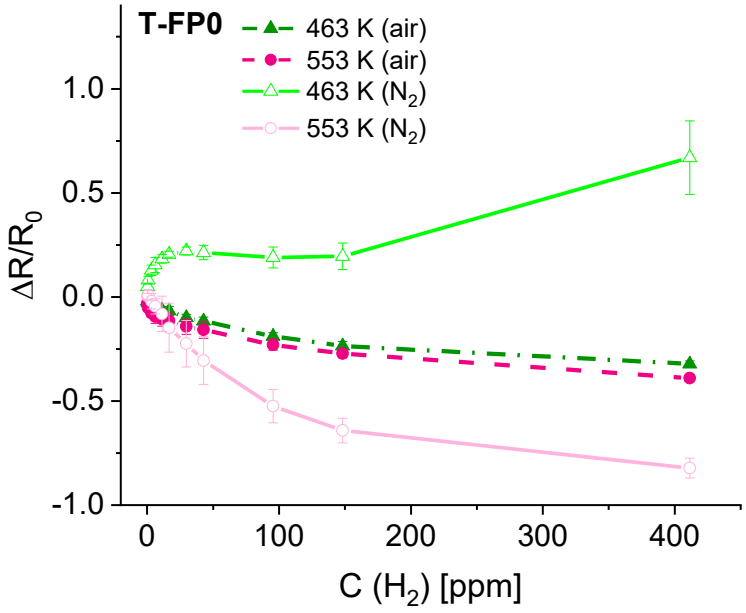

Figure S24. Comparison of the response of sample T-FP0 to hydrogen gas, measured in air and nitrogen atmospheres at 463 K and 553 K. Measurements in air are shown with dashed or dotted lines: dark green triangles with a dash-dot line represent 463 K, and pink circles with dashes represent 553 K. Measurements in nitrogen are shown with solid lines: light green triangles represent 463 K, and light pink circles represent 553 K. The error bars represent the propagated uncertainties in the response, calculated from the standard deviations of R and R_0, and their covariance.

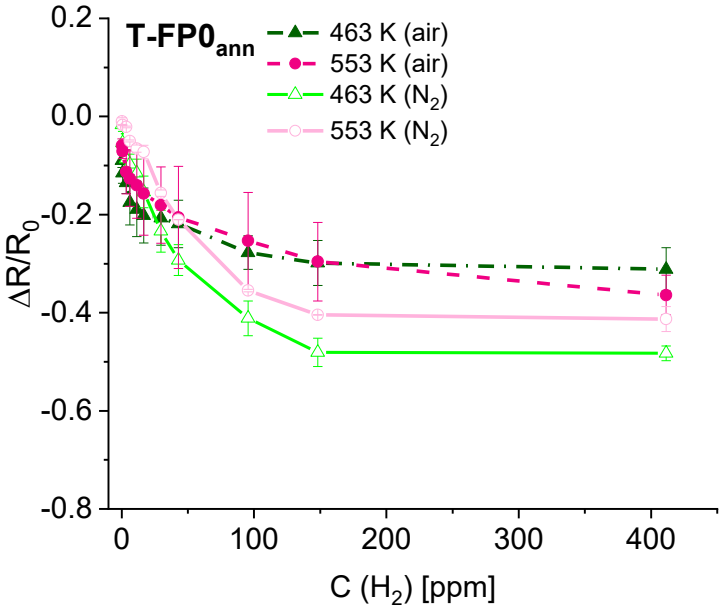

Figure S25. Comparison of the response of sample T-FP0$_{ann}$ to hydrogen gas, measured in air and nitrogen atmosphere at 463 K and 553 K. Measurements made in air are shown with dashed or dotted lines: dark green triangles with a dash-dot line represent 463 K, pink circles with dashes represent 553 K. Measurements in nitrogen are shown with solid lines: light green triangles represent 463 K, light pink circles represent 553 K. The error bars indicate the propagated uncertainties in the response, calculated from the standard deviations of R and R_0, and their covariance.

References

1 M. Šoltić, Z. Klencsár, G. Dražić, M. Gotić, M. Ivanda, N. Baran, Hydrogen gas sensing properties of mechanochemically dispersed platinum on α-Fe_2O_3 support, *Sens. Actuators A: Phys*., 2024, **376**, 115539.

2 R. Hesse, T. Chassé T., R. Szargan, Peak shape analysis of core level photoelectron spectra using UNIFIT for WINDOWS, *Fresenius J. Anal. Chem*., 1999, **365**, 48–54.

3 G. Held, F. Venturini, D.C. Grinter, P. Ferrer, R. Arrigo, L. Deacon, W. Quevedo Garzon, K. Roy, A. Large, C. Stephens, A. Watts, P. Larkin, M. Hand, H. Wang, L. Pratt, J.J. Mudd, T. Richardson, S. Patel, M. Hillman, S. Scott, Ambient-pressure endstation of the Versatile Soft X-ray (VerSoX) beamline at Diamond Light Source, *J. Synchrotron Radiat.,* 2020, **27**, 1153–1166.

4 D.C. Grinter, F. Venturini, P. Ferrer, M.A. van Spronsen, R. Arrigo, W. Quevedo Garzon, K. Roy, A.I. Large, S. Kumar, G. Held, The Versatile Soft X-Ray (VerSoX) Beamline at Diamond Light Source, *Synchrotron Radiat. News,* 2022, **35**, 39–47.

5 F. Jiménez-Villacorta, C. Prieto, Y. Huttel, N.D. Telling, G. Van Der Laan, X-ray magnetic circular dichroism study of the blocking process in nanostructured iron-iron oxide core-shell systems, *Phys. Rev. B,* 2011, **84**, 172404.

6 K. Lagarec, D. G. Rancourt, Extended Voigt-based analytic lineshape method for determining N-dimensional correlated hyperfine parameter distributions in Mössbauer spectroscopy, *Nucl. Instrum. Methods Phys. Res. B*, 1997, **129**, 266–280.

7 I. Marić, M. Šoltić, G. Dražić, M.A. van Spronsen, G. Štefanić, M. Ivanda, G. Held, T. Jurkin, K. Bohinc, M. Gotić, Synthesis of Pt decorated manganese oxide (MnO_2/Mn_5O_8) nanorods and their catalytic activity for the reduction of 4-nitrophenol to 4-aminophenol, *Appl. Surf. Sci.,* 2024, **649**, 159091.

8 X.F. Lu, X.Y. Chen, W. Zhou, Y.X. Tong, G.R. Li, α-Fe_2O_3@PANI core-shell nanowire arrays as negative electrodes for asymmetric supercapacitors, *ACS Appl. Mater. Interfaces.,* 2015, **7**, 14843–14850.

9 J.-C. Wang, J. Ren, H.-C. Yao, L. Zhang, J.-S. Wang, S.-Q. Zang, L.-F. Han, Z.-J. Li, Synergistic photocatalysis of Cr(VI) reduction and 4-Chlorophenol degradation over hydroxylated α-Fe_2O_3 under visible light irradiation, *J. Hazard. Mater.,* 2016, **31**, 11–19.

10 G. Zhuang, Y. Chen, Z. Zhuang, Y. Yu, J. Yu, Oxygen vacancies in metal oxides: recent progress towards advanced catalyst design, *Sci. China. Mater.*, 2020, **63**, 2089–2118.

11 X. Li, S. Li, Y. Cheng, L. Zheng, L. Song, X. Zi, H. Dai, The Activation of Oxygen Species on the Pt/CeO_2 Catalyst by H_2 for NO Oxidation, *Catal.,* 2024, **14**, 778.

12 M. Favaro, H. Xiao, T. Cheng, W.A. Goddard III, J. Yano, E.J. Crumlin, Subsurface oxide plays a critical role in CO_2 activation by Cu(111) surfaces to form chemisorbed CO_2, the first step in reduction of CO_2, *Proc. Natl. Acad. Sci. U.S.A.,* 2017, **114**, 6706–6711.

13 H. Bluhm, M. Hävecker, A. Knop-Gericke, E. Kleimenov, R. Schlögl, D. Teschner, V.I. Bukhtiyarov, D.F. Ogletree, M. Salmeron, Methanol oxidation on a copper catalyst investigated using in situ X-ray photoelectron spectroscopy, *J. Phys. Chem. B.,* 2004, **108**, 14340–14347.

14 J.-L. Grosseau-Poussard, B. Panicaud, F. Pedraza, P.O. Renault, J.-F. Silvain, Iron oxidation under the influence of phosphate thin films, *J. Appl. Phys.,* 2003, **94**, 784–788.

15 S. Zhang, X. Chang, L. Zhou, X. Liu, J. Zhang, Stabilizing Single-Atom Pt on Fe_2O_3 Nanosheets by Constructing Oxygen Vacancies for Ultrafast H_2 Sensing, *ACS Sens.,* 2024, **9**, 2101–2109.

16 M. Lin, L. Tng, T. Lim, M. Choo, J. Zhang, H.R. Tan, S. Bai, Hydrothermal synthesis of octadecahedral hematite (α-Fe_2O_3) nanoparticles: An epitaxial growth from goethite (α-FeOOH), *J. Phys. Chem. C,* 2014, **118**, 10903–10910..

17 A. Rufus, N. Sreeju, D. Philip, Synthesis of biogenic hematite (α-Fe_2O_3) nanoparticles for antibacterial and nanofluid applications, *RSC Adv.,* 2016, **6**, 94206–94217.

18 A.A. Qureshi, S. Javed, H.M.A. Javed, M. Jamshaid, U. Ali, M.A. Akram, Systematic Investigation of Structural, Morphological, Thermal, Optoelectronic, and Magnetic Properties of High-Purity Hematite/Magnetite Nanoparticles for Optoelectronics, *Nanomater.* 2022, **12**, 1635.

19 R. Zboril, M. Mashlan, D. Petridis, Iron(III) oxides from thermal processes-synthesis, structural and magnetic properties, Mössbauer spectroscopy characterization, and applications, *Chem. Mat.,* 2002, **14**, 969–982.

20 F. Bødker, S. Mørup, Size dependence of the properties of hematite nanoparticles, *Europhys. Lett.,* 2000, **52**, 217-223.

21 M.-Z. Dang, D.G. Rancourt, J.E. Dutrizac, G. Lamarche, R. Provencher, Interplay of surface conditions, particle size, stoichiometry, cell parameters, and magnetism in synthetic hematite-like materials, *Hyperfine Interact.,* 1998, **117**, 271–319.

22 Morin F. J., Magnetic Susceptibility of α-Fe_2O_3 and α-Fe_2O_3 with Added Titanium, *Phys. Rev.,* 1950, **78**, 819–820.

23 F. van der Woude, Mössbauer Effect in α-Fe_2O_3, *Phy. Stat. Sol. (b),* 1966, **17**, 417–432.

24 T. Ruskov, T. Tomov, S. Georgiev, Mössbauer investigation of the Morin transition in hematite, *Phy. Stat. Sol. (a)*, 1976, **37**, 295–302.

25 C. Frandsen, S. Mørup, Spin rotation in α-Fe_2O_3 nanoparticles by interparticle interactions, *Phys. Rev. Lett.,* 2005. **94**, 027202.

26 M. Gracheva, Z. Homonnay, K. Kovács, K.A. Béres, J.C. Biondi, Y. Wenchao, V. Kovács Kis, I. Gyollai, M. Polgári, Mössbauer characterization of microbially mediated iron and manganese ores of variable geological ages, *Ore. Geol. Rev.,* 2021, **134**, 104124.

27 Ö. Özdemir, D.J. Dunlop, T.S. Berquó, Morin transition in hematite: Size dependence and thermal hysteresis, *Geochem. Geophys. Geosyst.,* 2008, **9**, Q10Z01.

28 R.E. Vandenberghe, E. De Grave, G. De Geyter, C. Landuydt, Characterization of goethite and hematite in a Tunisian soil profile by Mossbauer spectroscopy., *Clays Clay Miner.,* 1986, **34**, 275–280.

29 J.I. Pérez-Landazábal, C. Gómez-Polo, V. Recarte, S. Larumbe, V. Sánchez-Alarcos, M.F. Silva, E.A.G. Pineda, A.A.W. Hechenleitner, M.K. Lima, J.A. Rodriguez-Velamazán, Morin transition in Hematite nanoparticles analyzed by neutron diffraction, *J. Phys. Conf. Ser.,* 2015, **663**, 012003.

30 P. Pincus, Theory of magnetic resonance in α-Fe_2O_3, *Phys. Rev. Lett.,* 1960, **5**, 13–15.

31 C. Carbone, F. Di Benedetto, C. Sangregorio, P. Marescotti, L.A. Pardi, L. Sorace, Multifrequency EMR and magnetic characterization of synthetic powdered hematite, *J. Phys. Chem. C,* 2008, **112**, 9988–9995.

32 H. Kumagai, H. Abe, K. Ôno, I. Hayashi, J. Shimada, K. Iwanaga, Frequency dependence of magnetic resonance in α-Fe_2O_3, *Phys. Rev.,* 1955, **99**, 1116–1118.

33 P.W. Anderson, F.R. Merritt, J.P. Remeika, W.A. Yager, Magnetic resonance in α-Fe_2O_3, *Phys. Rev.,* 1954, **93**, 717–718.

34 M. Vasquez Mansilla, R. Zysler, D. Fiorani, L. Suber, Annealing effects on magnetic properties of acicular hematite nanoparticles, *Phys. B: Condens. Matter.,* 2002, **320**, 206-209.

35 N. Goel, K. Kunal, A. Kushwaha, M. Kumar, Metal oxide semiconductors for gas sensing, *Eng. Rep.,* 2023, **5**, e12604.

36 Shrisha, C.-M. Wu, K.G. Motora, G.-Y. Chen, D.-H. Kuo, N.S. Gultom, Highly efficient reduced tungsten oxide-based hydrogen gas sensor at room temperature, *Mater. Sci. Eng. B,* 2023, **289**, 116285.

37 S. M. Merah, Y. Bakha, A. Djelloul, N-type and P-type SnO_x thin films based MOX gas sensor testing, *J. Mater. Sci: Mater. Electron.*, 2024, **35**, 250.

38 R.B. T, P.V.K. Yadav, A. Mondal, K. Ramakrishnan, J. Jarugala, C. Liu, Y.A.K. Reddy, Enhanced response of WO_3 thin film through Ag loading towards room temperature hydrogen gas sensor, *Chemosphere,* 2024, **353**, 141545.

39 S. Mobtakeri, S. Habashyani, H.F. Budak, E. Gür, High responsive Pd decorated low temperature α-MoO_3 hydrogen gas sensor, *Ceram. Int.,* 2024, **50**, 38761–38768.

40 A. A. Haidry, L. Xie, Z. Wang and Z. Li, Hydrogen sensing and adsorption kinetics on ordered mesoporous anatase TiO_2 surface, *Appl. Sur.f Sci.*, 2020, **500**, 144219.

41 N. X. Thai, N. Van Duy, N. Van Toan, C. M. Hung, N. Van Hieu and N. D. Hoa, Effective monitoring and classification of hydrogen and ammonia gases with a bilayer Pt/SnO_2 thin film sensor, *Int. J. Hydrogen Energy*, 2020, **45**, 2418–2428.

42 G. Pandey, M. Bhardwaj, S. Kumar, S. D. Lawaniya, M. Kumar, P. K. Dwivedi, K. Awasthi, Synergistic effects of Pd-Ag decoration on SnO/SnO_2 nanosheets for enhanced hydrogen sensing, *Sens. Actuators B Chem.*, 2024, **402**, 135062.

43 X.-T. Yin, Z.-Y. Yang, D. Dastan, Y. Liu, X.-M. Tan, X.-C. Gao, Y.-W. Zhou, J. Li, X.-G. Ma, Sensitivity and selectivity Pt loaded SnO_2–Co_3O_4 gas sensor for hydrogen detection, *Ceram. Int.*, 2023, **49**, 38717–38725.

44 M. Guo, X. Li, L. Wang, Z. Xue, J. Xu, Redispersing Ir nanoparticles via a carbon-assisted pyrolysis process to break the activity−stability trade-off of H_2 sensors, *ACS Sens.*, 2024, **9**, 3327–3337.